

<https://helda.helsinki.fi>

Sonophotocatalytic degradation of sulfadiazine by integration of microfibrillated carboxymethyl cellulose with Zn-Cu-Mg mixed metal hydroxide/g-C₃N₄ composite

Gholami, Peyman

2020-08-15

Gholami , P , Khataee , A , Vahid , B , Karimi , A , Golizadeh , M & Ritala , M 2020 , ' Sonophotocatalytic degradation of sulfadiazine by integration of microfibrillated carboxymethyl cellulose with Zn-Cu-Mg mixed metal hydroxide/g-C₃N₄ composite ' , Separation and Purification Technology , vol. 245 , 116866 . <https://doi.org/10.1016/j.seppur.2020.116866>

<http://hdl.handle.net/10138/347039>

<https://doi.org/10.1016/j.seppur.2020.116866>

cc_by_nc_nd

acceptedVersion

Downloaded from Helda, University of Helsinki institutional repository.

This is an electronic reprint of the original article.

This reprint may differ from the original in pagination and typographic detail.

Please cite the original version.

**Sonophotocatalytic degradation of sulfadiazine by integration of
microfibrillated carboxymethyl cellulose with Zn-Cu-Mg mixed metal
hydroxide/g-C₃N₄ composite**

Peyman Gholami,^a Alireza Khataee,^{b,c,d,} Behrouz Vahid,^e Afzal Karimi,^f Mortaza Golizadeh,^g
Mikko Ritala^a*

^a Department of Chemistry, University of Helsinki, P.O. Box 55, Helsinki 00014, Finland

^b Research Laboratory of Advanced Water and Wastewater Treatment Processes, Department of Applied Chemistry, Faculty of Chemistry, University of Tabriz, 51666-16471 Tabriz, Iran

^c Department of Environmental Engineering, Gebze Technical University, 41400 Gebze, Turkey

^d Institute of Research and Development, Duy Tan University, Da Nang 550000, Vietnam

^e Department of Chemical Engineering, Tabriz Branch, Islamic Azad University, Tabriz, Iran

^f Faculty of Advanced Technologies in Medicine, Iran University of Medical Sciences, 14496-14535 Tehran, Iran

^g Chemical and Petroleum Engineering Department, Sharif University of Technology, Tehran, 14588-89694, Iran

* Corresponding author:

Email: a_khataee@tabrizu.ac.ir

Abstract

This research aimed to prepare a recoverable sonophotocatalyst, in which microfibrillated carboxymethyl cellulose (MFC) acted as the Zn-Cu-Mg-mixed metal hydroxide/graphitic carbon nitride (MMH/g-C₃N₄) carrier. The characteristics of bare and composite sonophotocatalysts were analyzed by the XRD, FT-IR, BET, DRS, PL and FE-SEM equipped with the EDX mapping. The performance of prepared composites (MMH/g-C₃N₄@MFC) with various weight ratios of the MMH/g-C₃N₄ was studied for the sonophotocatalytic degradation of sulfadiazine (SDZ) as the model emerging contaminant. 93% of SDZ was degraded using the most effective catalyst (MMH/g-C₃N₄@MFC₃) with 15% weight ratio of the MMH/g-C₃N₄ under the desired operating conditions including solution pH of 6.5, SDZ concentration of 0.15 mM and ultrasonic power of 300 W. The MMH addition to the g-C₃N₄ structure increased the separation of charge carriers generated via the visible light or ultrasound irradiations. Moreover, the MMH/g-C₃N₄ was dispersed uniformly on the MFC and consequently, more active sites were available to form reactive oxygen species (ROS), compared to powder form. Hydroxyl radicals ([•]OH) were determined as the main ROS in the SDZ degradation by performing a series of scavenging experiments. Less than 10% decrease in the degradation efficiency of SDZ was observed during five subsequent experiments, which indicated the proper retention of the MMH/g-C₃N₄ particles in the MFC. The adequate mineralization of SDZ (83% decrease in chemical oxygen demand (COD)) was obtained after 200 min of treatment. Eventually, ten degradation intermediates were identified by the GC-MS analysis and a plausible degradation mechanism for the contaminant was proposed.

Keywords: Antibiotic degradation; Composite; Graphitic carbon nitride; Microfibrillated carboxymethyl cellulose; Mixed metal hydroxide; Sonophotocatalysis.

1. Introduction

The increasing consumption of antibiotics, anticonvulsants, antipyretics, hormones and cytostatics increases annually and, consequently, their presence in natural water sources and industrial wastewaters has turned into the global challenge [1]. The removal of pharmaceuticals via conventional processes such as biological, physical and chemical methods is restricted due to their high persistence and low level in the wastewaters [2]. For instance, sulfadiazine (SDZ) as a non-biodegradable and stable sulfonamide antibiotic used for treatment of toxoplasmosis in animals and humans can be detected in effluents of domestic, agricultural and industrial sectors [3]. If these waters are used for the irrigation, such pollutants will enter the food chain through interaction with the soil resulting in serious consequences. Hence, the SDZ degradation in the wastewaters by efficient novel techniques is important from the practical and environmental points of view [3].

Photocatalysis and sonocatalysis, as advanced oxidation processes (AOPs), can be applied with proper catalysts for degradation of many hazardous pollutants owing to the high ability of these methods in mineralization of refractory chemicals [4, 5]. Furthermore, various AOPs can be combined for their synergistic effects in the pollutants degradation [6]. For instance, the sonophotocatalytic process as an AOP can be applied for the degradation of various pollutants in wastewaters [4, 6]. The mechanism of the sonolysis is based on the cavitation phenomenon forming microbubbles in a liquid, which grow by absorbing energy from the ultrasonic field to a transient size and then collapse to form localized microreactors with high temperatures and pressures; as a result, H₂O molecules are dissociated in the aqueous solution to form $\cdot\text{OH}$ radicals [7, 8]. A semiconductor can be stimulated through the appropriate light or ultrasonic irradiations to form electron and hole (e^-/h^+) pairs in its conduction and valance bands, respectively, which also subsequently form reactive oxygen species (ROS) [6, 9].

Graphitic carbon nitride (g-C₃N₄) as the metal-free conjugated polymer with semiconductor property has been applied recently as the photocatalyst owing to its suitable traits including

narrow band gap (2.7 eV), adequate stability, low-price, proper potentials of band edges and non-toxicity [10]. However, its practical usage is restricted owing to its low efficiency of light absorption and surface area, as well as quick recombination of charge carriers which proceeds faster than the desired surface redox reactions [10]. Fabrication of heterojunctions through combining g-C₃N₄ with mixed metal oxides and hydroxides yields modified catalysts with desired optical properties, high surface area and stability [11-13]. It should be noticed that the hydroxyls in the metal hydroxides can increase the electron transfer, charge separation and thereby enhance the charge carrier lifetime [14-16]. Especially, Zn, Cu and Mg containing metal hydroxides have been reported as highly efficient, stable and low-cost semiconductors, which can be coupled with the g-C₃N₄ to reduce the recombination rate of charge carriers [11, 17, 18]. However, such composites have some obstacles for their applications like retention of particles in the reactor vessel, high-cost, hard recycling, low reusability and aggregation [19].

Retaining of photocatalyst powder in suitable materials like microfibrillated carboxymethyl cellulose (MFC) has been actively investigated. The inexpensive, recyclable and biodegradable MFC is a natural fibrous network with high surface area and strength for the photocatalyst integration compared to the conventional wooden fibers [19, 20]. Hence, MFC can be applied to form composites with desired properties and structures. Moreover, the amount and aggregation property of a photocatalyst in the MFC affect the photocatalytic activity of the composite in the exposure of the ultrasound and visible light irradiations [19].

In this study, the MFC is investigated as a carrier for Zn-Cu-Mg-mixed metal hydroxide-g-C₃N₄ (MMH/g-C₃N₄) to produce water resistant fibrous composites (MMH/g-C₃N₄@MFC) of varying MMH/g-C₃N₄ loading. The composite characteristics were investigated by X-ray diffraction (XRD), Fourier transform infrared (FT-IR) spectroscopy, N₂ adsorption-desorption analyzed by the Brunauer-Emmett-Teller (BET) technique, diffuse reflectance spectroscopy (DRS), photoluminescence (PL) spectroscopy and field emission scanning electron microscopy

(FE-SEM) equipped with energy dispersive X-ray (EDX) mapping. The catalytic activity of the prepared composites with different MMH/g-C₃N₄ loadings was monitored by measuring the degradation efficiency of SDZ solutions under visible light and ultrasound irradiation. Effects of the main operational parameters and free radical enhancers and scavengers on the pollutant degradation were also investigated. Eventually, catalyst reusability, intermediates of the pollutant degradation, and mineralization efficiency were investigated under the optimized conditions, and degradation pathways were proposed.

2. Materials and methods

2.1. Reagents and chemicals

Copper(II) chloride (CuCl₂: 99%), zinc chloride (ZnCl₂: ≥98%), melamine (C₃H₆N₆: 99%), magnesium chloride hexahydrate (MgCl₂·6H₂O: 99%), sodium sulfate (Na₂SO₄: 98.5%), sodium hydroxide (NaOH: 99%), nitric acid (HNO₃: 65%), hydrogen peroxide (H₂O₂: 35%), potassium persulfate (K₂S₂O₈: ≥ 99%), n-butanol (C₄H₁₀O > 99.7%), hydrochloric acid (HCl: 37%), sulfuric acid (H₂SO₄: 98%), sodium carbonate (Na₂CO₃: 98%), ethylenediamine tetraacetic acid (EDTA, C₁₀H₁₆N₂O₈: 99%), 1,4-benzoquinone (C₆H₄O₂: 99%) were provided from Merck (Germany). SDZ was purchased from Sobhan Company (Iran). All mentioned chemicals were applied as received with no purification and the SDZ solutions were made by Millipore water.

2.2. Preparation of g-C₃N₄, MMH and MMH/g-C₃N₄

Graphitic carbon nitride was prepared based on an extensively used method [21]. Briefly, melamine powder (5 g) was calcined in an alumina crucible with a cover (520 °C for 2 h), and the temperature was increased to 540 °C for further 2 h. The obtained product with a yellow color was grinded for further application.

In order to synthesize MMH/g-C₃N₄ composite, 0.1 g of g-C₃N₄ was sonicated in a solution (500 mL) containing MgCl₂·6H₂O (0.125 M), CuCl₂ (0.125 M) and ZnCl₂ (0.250 M) for 2 h. Then, a stoichiometric amount of NaOH (1L, 0.05 M, 2.0 mL/min) was added; the solution pH had to be lower than 10 during this procedure to prevent the transformation to metal oxides. The resulted precipitate was filtered, washed and dried (60 °C, 48 h). MMH was prepared by an identical procedure in the absence of g-C₃N₄.

2.3. Preparation of MMH/g-C₃N₄@MFC film

Carboxymethyl cellulose (2% w/v) was dissolved in a solution of glycerin (0.5% v/v) and distilled water by mixing until the solution became clear. MMH/g-C₃N₄ at various weight ratios of 5, 10 and 15% to the MFC was added to the solution and the obtained suspension was sonicated for 15 min. Next, the homogeneous suspension was poured on a glass plate and air dried (24 h), afterwards the formed film was picked up from the glass and soaked in Al₂(SO₄)₃ (1% w/v) for cross-linking (1 h). Ionic crosslinking is an efficient method that couples ionizable polymers with divalent and/or trivalent cations. Carboxymethyl cellulose can form strong hydrogels in the presence of trivalent cations such as Al³⁺ or Fe³⁺. These cations interact with the carboxylate groups in the carboxymethyl cellulose backbone to form ionic crosslinks (Fig. S1). Al₂(SO₄)₃ has been widely used as a cross-linking agent in the preparation of biomaterials exhibiting excellent performance and low toxicity [22]. The resulted film was washed with distilled water to eliminate remaining ions, and then dried and cut in uniform strips (2.5 cm × 2.5 cm). Three composites with various weight ratios of MMH/g-C₃N₄ (5, 10 and 15%) were prepared and studied in the sonophotocatalyst tests, abbreviated as the MMH/g-C₃N₄@MFC₁, MMH/g-C₃N₄@MFC₂ and MMH/g-C₃N₄@MFC₃, respectively.

2.4. Characterization

The prepared samples were identified and characterized by the XRD using a Panalytical X'pert diffractometer (Cu K α radiation: 0.15406 nm; 45 kV, 40 mA, the Netherlands). FE-SEM (Tescan, Mira III, Czech Republic) with the EDX mapping was used to study the atomic distribution and morphology of the samples. FT-IR spectra of the samples were measured with a Bruker Tensor 27 analyzer (Germany). A Sinco S-4100 UV-Vis spectrophotometer (South Korea) was used to measure UV-Vis DRS spectra for determining and comparing the band gaps. Nitrogen adsorption–desorption isotherms were measured at 77 K using a Belsorp instrument (Mini II, Japan). PL spectroscopy was carried out by a Perkin Elmer LS45 spectrometer (USA).

2.5. Sonophotocatalytic activity assessment

The SDZ solution was ultrasonicated using an ultrasound bath (40 kHz, 300 W, Sonica, EP S3, Italy) in the exposure to LED lamp with visible light irradiation (15 W). First, a distinct dosage of the prepared catalyst was poured into the SDZ solution (150 mL) and stirred for 30 min under dark condition. Next, the solution was placed in an ultrasound bath (100 min). During the treatment process, the solution was extracted (3 mL) at 20-min intervals. The SDZ absorbance was measured by a spectrophotometer (SU-6100, Philler scientific, USA). In each measurement, the absorbance of the solution was used to calculate the SDZ degradation efficiency (DE (%)) at a given time of the treatment process [23]. In order to identify the intermediates formed within the SDZ decomposition, an Agilent 6890 gas chromatograph (GC) equipped with an Agilent 5973 mass spectrometer (MS) was utilized based on our previous work of the sample preparation and the subsequent GC-MS method [24]. Chemical oxygen demand (COD) was determined to evaluate the SDZ mineralization after the sonophotocatalysis process using Palintest instrument (United Kingdom) according

to American Public Health Association (APHA) standard method [25]. Ionic by-products such as SO_4^{2-} , NO_3^- and NH_4^+ ions generated in the SDZ degradation were also measured by an ion chromatography system (930 Compact IC Flex, Metrohm, Switzerland).

3. Results and discussion

3.1. Characterization of $g-C_3N_4$, MMH, MMH/ $g-C_3N_4$ and MMH/ $g-C_3N_4@MFC_3$

The XRD analyses were carried out to characterize the $g-C_3N_4$, MMH and MMH/ $g-C_3N_4$ samples (Fig. 1 (a)). Two representative (100) and (002) diffraction peaks at $2\theta = 13.3^\circ$ and 27.3° confirmed the proper production of $g-C_3N_4$ (JCPDS 87-1526). Moreover, Fig. 1 (a) illustrates the XRD pattern of the MMH, in which the characteristic diffraction peaks of the orthorhombic $Cu(OH)_2$ (JCPDS card No 80-656), the hexagonal brucite $Mg(OH)_2$ (JCPDS card No. 7-239) and the orthorhombic $Zn(OH)_2$ (JCPDS card No 20-1435) can be recognized. Eventually, based on what is clear from the XRD patterns of the MMH/ $g-C_3N_4$ composite, all of the peaks identified in both the pristine $g-C_3N_4$ and MMH diffractograms can be observed in the XRD pattern of the composite and no impurities were detected.

To study the functional groups of the as-prepared samples ($g-C_3N_4$, MMH, MMH/ $g-C_3N_4$ and MMH/ $g-C_3N_4@MFC_3$), the FT-IR analyses were performed and the results are presented in Fig. 1 (b). The peaks observed at about 3350, 2950 and 1720 cm^{-1} are related to the O-H, C-H and C=O stretching vibrations [26]. The peak at the wavenumber of 1614 cm^{-1} is associated with the aromatic ring quadrant stretch modes [27]. In addition, the bands at 1530 and 1126 cm^{-1} correspond to the stretching vibrations of C=N and C-N bonds, respectively [28, 29]. The peak at 1424 cm^{-1} is mainly owing to the bending vibration of CH_2 bonds [30]. The band in the $500-1000\text{ cm}^{-1}$ range is from the M-OH and M-O stretching vibrations (M: mentioned metals) [31, 32].

Isotherms of the N₂ adsorption-desorption were used to determine the surface area of the g-C₃N₄, MMH and MMH/g-C₃N₄ samples by the BET technique (Fig. 1 (c)). All the samples exhibited Type IV isotherms with a broad H2 type hysteresis loop for relative pressures higher than 0.4. According to the IUPAC classification, these kinds of isotherms demonstrates the mesoporous structure with narrow pore size distribution and slit-shaped pores [33]. In comparison with the bare g-C₃N₄ (specific surface area = 42 m²/g and pore volume = 0.17 m³/g), MMH (specific surface area = 64 m²/g and pore volume = 0.22 m³/g) and MMH/g-C₃N₄ (specific surface area = 54 m²/g and pore volume = 0.21 m³/g) presented better textural characteristics.

The optical properties of the g-C₃N₄, MMH and MMH/g-C₃N₄ composite were determined using the UV-Vis DRS spectroscopy (Fig. 1 (d)). To measure the band gaps of the as-prepared catalysts, the linear part of $(\alpha h\nu)^2$ versus $(h\nu)$ plot was extrapolated where α and $h\nu$ are the absorption coefficient and the photon energy (eV), respectively [34]. Based on Fig. 1 (d), the band gaps of g-C₃N₄, MMH and MMH/g-C₃N₄ composite were 2.7, 3.2 and 2.8 eV, respectively. The results of the SDZ decomposition (Section 3.2) display the significant role of the MMH in the prepared composites, which led to the improved catalytic activity compared to the bare g-C₃N₄ through a prevention of the electron-hole recombination during the sonophotocatalytic process, as will be discussed elaborately in the mentioned part [35].

The PL spectroscopy was applied to evaluate the charge carrier behavior in the g-C₃N₄ and MMH/g-C₃N₄ and to demonstrate the effect of MMH on the g-C₃N₄ catalytic activity. As shown in Fig. 1 (e), an emission peak at 455 nm appears for the g-C₃N₄ owing to the band-band transition of the photogenerated charge carrier. The pristine g-C₃N₄ demonstrated higher emission intensity in the PL, and loading of the MMH resulted in a reduced PL emission intensity. This decrease can be related to the improved electron-hole separation because of the junction formed between the MMH and g-C₃N₄. These results demonstrate the function of

MMH in the charge separation and transfer at the interface for the enhanced catalytic performance [36].

Fig. 2 displays the morphologies and microstructures of the g-C₃N₄, MMH, MMH/g-C₃N₄, and MMH/g-C₃N₄@MFC₃ samples. The bare g-C₃N₄ powder showed the typical aggregated flake-like morphology (Fig. 2 (a-c)) whereas the bare MMH powder had a regular cubic-shape appearance with 150-700 nm edge lengths (Fig. 2 (d-f)). The FE-SEM images of the MMH/g-C₃N₄ composite present the cubic-shaped MMH microparticles attached to the g-C₃N₄ (Fig. 2 (g-i)). Fig. 2 (j and k) demonstrate representative SEM images of the bare MFC. The carboxymethyl cellulose fibers showed smooth surfaces and were approximately 15 μm in diameter. Clearly, the structure of MFC has adequate space for the immobilization of MMH/g-C₃N₄ particles. The SEM images of MMH/g-C₃N₄@MFC₃ in Fig. 2 (l-o) indicate that the surface morphology of the MFC was altered obviously by modifying with the MMH/g-C₃N₄. As can be seen in Fig. 2l, the surface of the modified fiber became rougher than the pristine MFC. The SEM images of MMH/g-C₃N₄@MFC₃ with various magnifications demonstrate that the MMH/g-C₃N₄ particles were uniformly dispersed on the MFC surface without aggregation.

To study the elemental distributions in the various samples, the EDX elemental mapping analysis was carried out for the bare MFC and MMH/g-C₃N₄@MFC composites (Fig. 3). The EDX map of the bare MFC and the related quantitative results are shown in Fig. 3 (a1-a3) and Table S1, respectively, which confirmed the presence of C (48%) and O (52%) elements in the bare MFC without any impurities as expected. However, the EDX maps of the MMH/g-C₃N₄@MFCs with different MMH/g-C₃N₄ amounts show also the presence of Zn, Mg and Cu elements in addition to the C, N and O with various contents of the mentioned metals in the different samples. The observed difference in the distribution of the metals owes to the different MMH/g-C₃N₄ contents used for the composites preparation. The MMH/g-C₃N₄@MFC₁ with 5% weight ratio of MMH/g-C₃N₄ showed the lowest contents for the Zn, Mg and Cu whereas

the MMH/g-C₃N₄@MFC₃ with 15% weight ratio of the MMH/g-C₃N₄ demonstrated the highest contents for them (Table S1). These results also confirmed the successful preparation of the final composites as the sonophotocatalysts.

3.2. Comparison of the efficiency of different methods for the SDZ removal

Function of each constituent of the final composite as well as the role of visible light and sonication in the SDZ removal were investigated by performing some preliminary tests. Based on the obtained results (Fig. 4 (a)), low pollutant removal was observed using visible light (5%), sonolysis (9%) and ultrasound/visible (12%) irradiations in the absence of any catalysts within 100 min reaction time. For the sonophotocatalysis, the catalyst suspension was stirred for 30 min under the dark condition to reach the adsorption-desorption equilibrium. Less than 6% SDZ removal was observed after 30 min stirring in the presence of different catalysts. In contrast, the combined visible light and ultrasound irradiations in the presence of MMH and g-C₃N₄ led to higher SDZ degradation (41% and 63%, respectively) compared to the sole sonophotolysis (12%). The SDZ degradation efficiency was remarkably enhanced using the MMH/g-C₃N₄ composite as the sonophotocatalyst (88%). The catalytic characteristics of g-C₃N₄ derive from the narrow band gap (2.7 eV) and high photosensitivity [10, 37]. Furthermore, the improved sonophotocatalytic activity of g-C₃N₄ modified with the MMH is attributed to the lower electron–hole recombination rate of the sono- or photogenerated charge carriers and consequent increment in their lifetime [14, 36]. Based on the results of the PL analysis, the MMH addition to the g-C₃N₄ structure declined the recombination of e⁻ and h⁺ pairs. In addition, the superior sonophotocatalytic performance of the MMH/g-C₃N₄ composite can be ascribed to its larger specific surface area, which provides more active sites to improve the reaction rate. Interestingly, the embedment of the MMH/g-C₃N₄ into the MFC formed proper composite catalysts which could remove 51%, 82% and 93% of SDZ when exposed to

the visible light and ultrasound irradiations in the case of MMH/g-C₃N₄@MFC₁, MMH/g-C₃N₄@MFC₂ and MMH/g-C₃N₄@MFC₃, respectively (Fig. 4 (c)).

When the MMH/g-C₃N₄ was incorporated into the MFC fibrous network, the aggregated particles were uniformly dispersed on MFC resulting in extra active sites to produce more reactive oxygen species and consequently increased the SDZ degradation efficiency [19]. Moreover, the ultrasound waves caused more cavitation bubbles in the presence of the solid catalysts due to the lower solid-liquid tensile strength, which led to a higher water dissociation and sonoluminescence [38]. The sonoluminescence is the emission of light through the free radical recombination in the cavitation microbubbles; and this light can also excite the semiconductor [38, 39]. The turbulence generated by the sonication promoted the transfer of mass from the solution to the catalyst surface [38]. On the other hand, the penetration of visible light and ultrasound waves were improved in the immobilized system compared to the suspension due to the scattering from the solid particles in the latter [40, 41]. Eventually, it should be mentioned that the use of MMH/g-C₃N₄@MFC is more convenient from the practical point of view because there is no need for separation of the suspension particles from the solution owing to the stabilization of the MMH/g-C₃N₄ particles into the MFC surface.

In the following, the SDZ degradation rate by the above-mentioned methods was evaluated kinetically. The results depicted in Fig. 4 (a and c) were fitted to the pseudo-first order kinetic model ($\ln \frac{A_0}{A} = k_{app} t$) and the rate constants (k_{app}) for the degradation reactions were estimated in Fig. 4 (b and d). As can be seen, the maximum k_{app} is achieved by the application of the MMH/g-C₃N₄@MFC₃ sonophotocatalyst for the SDZ removal. This indicates the significant role of the MFC in retaining the composite and the low electron-hole recombination rate achieved by coupling g-C₃N₄ with the MMH. As displayed in Fig. 4, the k_{app} values for the sole application of the g-C₃N₄ and MMH in the sonophotocatalytic process were 71×10^{-4} and 38×10^{-4}

4 min^{-1} , respectively, while the MMH/g-C₃N₄@MFC₃ had the k_{app} of $174 \times 10^{-4} \text{ min}^{-1}$ under the same operational conditions. The synergy effect from combining the different catalysts for the sonophotocatalytic process can be calculated from the estimated apparent reaction rate constants (Eq. 1) as 37%:

$$\text{Synergy (\%)} = \frac{k_{app\text{MMH/g-C}_3\text{N}_4\text{@MFC}_3} - (k_{app\text{g-C}_3\text{N}_4} + k_{app\text{MMH}})}{k_{app\text{MMH/g-C}_3\text{N}_4\text{@MFC}_3}} \quad (1)$$

3.3. Effect of experimental conditions on the degradation of SDZ

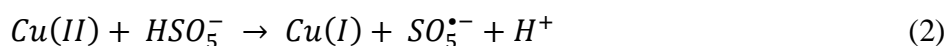
The effects of the initial SDZ concentration, pH and ultrasonic power were investigated to determine the optimized experimental conditions for the sonophotocatalysis of the target antibiotic using the MMH/g-C₃N₄@MFC₃ composite, which was found as the most effective sonophotocatalyst. Fig. 5 (a) shows the effect of the pollutant concentration on the degradation efficiency of SDZ; the DE% declined from 93 to 30% as the initial concentration of SDZ was increased from 15 to 35 mM. Higher amounts of $\cdot\text{OH}$ were needed when a higher SDZ concentration was present in the solution and, thereby, the same amounts of ROS generated at the identical operational conditions led to lower DE% with the increased initial pollutant concentration [42].

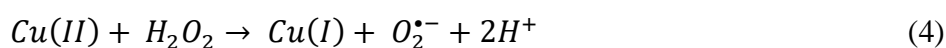
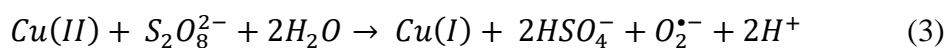
For the initial pH of the solution, as can be seen from Fig 5 (b), by changing the pH from 2.5 to 10.5 the degradation efficiency did not change considerably (less than 22%). This observation was due to the variations of composite surface and SDZ charges with the pH. The point of zero-charge (pH_{PZC}) of MMH/g-C₃N₄@MFC₃ was determined as 6.6, based on the salt addition method [43]. The surface charge of the catalyst was negative at $\text{pHs} > \text{pH}_{\text{PZC}}$. Furthermore, according to the pK_a of SDZ (6.5), the charge of SDZ was negative at $\text{pHs} > 6.5$ too [44]. Hence, at $\text{pH} \sim 6.5$, both the composite and SDZ are neutral and there was no repulsion between them, which led to the higher adsorption of SDZ on the catalyst surface to be oxidized

by the $\cdot\text{OH}$ radicals. The relatively lower SDZ degradation in the acidic and alkaline mediums was attributed to the repulsive interactions between the SDZ and the catalyst surface. Hence, the pH 6.5 as the natural pH of SDZ was selected for the subsequent experiments. Increasing the ultrasonic power from 150 to 300 W led to a higher SDZ degradation (Fig 5 (c)) owing to increased generation of cavitation microbubbles, which finally collapsed and generated more ROS due to the enhanced catalyst excitation by the sonication and sonoluminescence [45]. Moreover, mass transfer was promoted by the increased solution turbulence at higher dissipated energy entered to the medium. Finally, more unoccupied active sites existed on the catalyst surface compared to the absence of sonication [45, 46].

3.4. Enhancers and scavengers of reactive free radicals

To intensify the catalytic decomposition of the antibiotic pollutant, peroxydisulfate (PDS), peroxomonosulfate (PMS) and hydrogen peroxide (H_2O_2) as enhancers for generation of reactive oxygen species were added to the SDZ solution. In these tests, MMH/g- C_3N_4 @MFC₃ was applied for the degradation of SDZ (0.30 mM). All the enhancers generate additional reactive species such as sulfate and hydroxyl radicals which have remarkable oxidizing potential for the SDZ degradation [47]. DE% of 47% was observed in the absence of any enhancers. The presence of PDS, PMS and H_2O_2 enhancers led to the enhanced sonophotocatalytic degradation to 60%, 78% and 90%, respectively. Cu(II) ions on the MMH/g- C_3N_4 @MFC₃ surface can activate PMS to produce $\text{SO}_5^{\bullet-}$ (Eq. (2)) [48] and convert PDS and H_2O_2 to $\text{O}_2^{\bullet-}$ through Eqs. (3 and 4), respectively [49]. Furthermore, increasing the performance of the sonophotocatalysis by adding PDS and H_2O_2 can also be attributed to the improved formation of $\cdot\text{OH}$ and $\text{SO}_4^{\bullet-}$ radicals under ultrasound and visible light irradiation (Eqs. (5 and 6)) [46, 48].

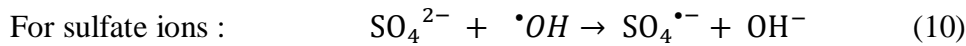
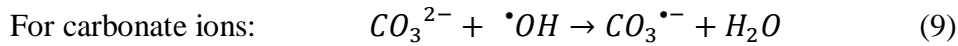
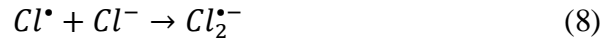
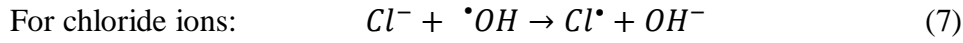




There are usually organic and inorganic compounds with radical scavenging effects in aqueous solutions. Hence, this effect on the SDZ sonophotocatalysis should be studied to evaluate the efficiency of the decomposition process in the solutions and the effects of various reactive radicals on the target pollutant [50]. Fig. 6 (b) demonstrates that the presence of t-butanol, EDTA and benzoquinone (BQ) resulted in unfavorable effects on the SDZ conversion. The t-butanol, BQ and EDTA are considered as scavengers for $\bullet OH$ radicals, superoxide radical anions ($O_2^{\bullet-}$) and holes (h^+), respectively [51-53]. Among these scavengers, t-butanol caused the highest prohibition for the sonophotocatalytic degradation of SDZ via direct elimination of $\bullet OH$ radicals. Hence, the SDZ degradation is mostly attributed to the $\bullet OH$ generation through the MMH/g-C₃N₄@MFC₃ under visible light. Comparatively, the $O_2^{\bullet-}$ had the lowest contribution to the pollutant degradation. Therefore, the following order was obtained for the SDZ degradation: $\bullet OH > h^+ > O_2^{\bullet-}$. It could be concluded that the holes also participated in the SDZ decomposition; the MMH in the final composite catalyst trapped the generated electrons in the conduction band and thus, the h^+ concentration in the valence band of g-C₃N₄ was enhanced for the improved SDZ degradation [54]; these results for the EDTA and BQ scavengers are in agreement with results reported by Ao *et al.* [55].

NaCl, Na₂SO₄ and Na₂CO₃ presented a particular degree of prohibiting effect on the degradation of the antibiotic pollutant (Fig. 6 (c)). The sonophotocatalytic decomposition of

SDZ decreased in the order of $\text{NaCl} > \text{Na}_2\text{SO}_4 > \text{Na}_2\text{CO}_3$ due to the following reactions, which scavenged $\cdot\text{OH}$ radicals and generated less active species [32, 50]:



Moreover, these scavengers could occupy the active sites of the $\text{MMH/g-C}_3\text{N}_4@\text{MFC}_3$ and as a consequence inhibit the excitation of the catalyst for the ROS generation for the efficient sonophotocatalysis [56].

3.5. *MMH/g-C₃N₄@MFC₃ reusability*

The reusability potential of the $\text{MMH/g-C}_3\text{N}_4@\text{MFC}_3$ sonophotocatalyst was investigated in order to determine the practical applicability of the catalyst. For this aim, the prepared composite was used in ten subsequent tests and the DE% was monitored. After each experiment, the film was washed with deionized water to remove any pollutant residue and dried. No mass loss or fracture in the catalyst structure was observed after the subsequent usage. The composite could easily be removed from the treated water and fully recycled. As shown in Fig. 7, around 5% decrease in the degradation efficiency of SDZ occurred by the end of the tenth experiment which demonstrates the proper stability of the composite sonophotocatalyst in repeated experiments. The results verified the proper capability of the $\text{MMH/g-C}_3\text{N}_4@\text{MFC}_3$ as a recyclable composite sonophotocatalyst.

3.6. Intermediates, mineralization and conversion of the SDZ

To recognize the intermediates formed within the sonophotocatalytic degradation of SDZ, the GC-MS analysis was implemented and the structures of the ten intermediates that could be identified are given in Table S2. Based on the identified by-products, two pathways can be considered for the SDZ conversion which started from the C–C, N–S and N–C bond cleavages (Fig. 8). In the first degradation pathway, the SDZ is destructed to the 2-nitropyrimidin and next, to the 1H-pyrimidin-2-one. In the subsequent step, the 1H-pyrimidin-2-one is transformed to aliphatic compounds like (3S)-3,4-diamino-4-oxobutanoic acid and N-carbamoylpropanamide. In the second degradation pathway, the SDZ is firstly degraded to 4-nitrophenol and then to benzene-1,4-diol and cyclohexa-2,5-diene-1,4-dione. Next, cyclohexa-2,5-diene-1,4-dione is decomposed to the aliphatic carboxylic acids like 2-methylpentanedioic acid and 3-hydroxypropanoic acid. In both pathways, the as-formed short chain compounds are eventually mineralized to H₂O and CO₂.

The chemical oxygen demand (COD) and ion chromatography (IC) analyses were carried out in the optimum operational conditions to study the efficiency of the SDZ sonophotocatalysis with the MMH/g-C₃N₄@MFC₃ composite. The COD results demonstrated 56% and 83% decrease in COD concentration after 100 and 200 min sonophotocatalysis, respectively. According to the IC analysis, the initial concentrations of SO₄²⁻ (0.1 mg L⁻¹), NH₄⁺ (0.5 mg L⁻¹) and NO₃⁻ (0.6 mg L⁻¹) ions increased to 2.6, 3.1 and 8.3 mg L⁻¹ during 100 min. This indicated the production of NH₄⁺ cations and SO₄²⁻ and NO₃⁻ anions as ionic by-products of the SDZ degradation. The COD decrease during the decomposition of SDZ as well as the generation of ionic species confirmed the proper progress of mineralization of SDZ as the antibiotic target pollutant [57].

4. Conclusions

MMH/g-C₃N₄ particles were incorporated into the MFC to form an effective composite catalyst. The MMH/g-C₃N₄@MFCs exhibited the highest sonophotocatalytic performance for the degradation of SDZ antibiotic-contaminated solutions due to the appropriate dispersion and retention of MMH/g-C₃N₄ particles on the MFC surface. Moreover, MMH prevented the rapid recombination of sonophotocatalytically produced holes and electrons. The ultrasonication increased the solution turbulence and consequently mass transfer to the catalyst surface. All the studied processes followed the pseudo-first order kinetics and the synergistic effect of the sonophotocatalysis with the MMH/g-C₃N₄@MFC₃ was calculated as 37%. The addition of radical enhancers improved the generation of the free oxidizing radicals and the SDZ sonophotocatalysis; vice versa trend was observed by the addition of radical scavengers, which confirmed the significant role of the reactive oxygen species, particularly hydroxyl radicals. Besides, negligible decline in the sonophotocatalytic activity of the MMH/g-C₃N₄@MFC₃ composite was seen after ten consecutive experiments. The adequate mineralization was also observed by monitoring the COD removal efficiency after 100 and 200 min of the SDZ treatment (56% and 83%, respectively), which was consistent with the IC analysis. The mechanism for the SDZ degradation was suggested based on the ten identified degradation intermediates. Conclusively, the as-prepared MMH/g-C₃N₄@MFC₃ composite catalyst is expected to be used for the effective treatment of antibiotic-polluted aqueous media under the ultrasound and visible light irradiations.

Acknowledgements

The authors acknowledge the support provided by the University of Tabriz and Iran University of Medical Sciences. The doctoral program in Materials Research and Nanosciences (MATRENA) of the University of Helsinki is thanked for financial support.

References

- [1] R. Karthik, J. Vinoth Kumar, S.-M. Chen, C. Karuppiah, Y.-H. Cheng, V. Muthuraj, A study of electrocatalytic and photocatalytic activity of cerium molybdate nanocubes decorated graphene oxide for the sensing and degradation of antibiotic drug chloramphenicol, *ACS Applied Materials & Interfaces*, 9 (2017) 6547-6559.
- [2] P. Chen, L. Wang, P. Song, X. Chen, Y. Yin, Y. Liu, L. Cai, L. Zhang, Recovering olaquinox and decreasing COD and salt concentrations in antibiotic wastewater by multiple freeze-thaw processes and crystallization, *Journal of Cleaner Production*, 225 (2019) 248-255.
- [3] F. Dong, C. Li, J. Crittenden, T. Zhang, Q. Lin, G. He, W. Zhang, J. Luo, Sulfadiazine destruction by chlorination in a pilot-scale water distribution system: Kinetics, pathway, and bacterial community structure, *Journal of Hazardous Materials*, 366 (2019) 88-97.
- [4] R. Abazari, A.R. Mahjoub, S. Sanati, Z. Rezvani, Z. Hou, H. Dai, Ni-Ti layered double hydroxide@graphitic carbon nitride nanosheet: A novel nanocomposite with high and ultrafast sonophotocatalytic performance for degradation of antibiotics, *Inorganic Chemistry*, 58 (2019) 1834-1849.
- [5] X. Zheng, J. Wang, J. Liu, Z. Wang, S. Chen, X. Fu, Photocatalytic degradation of benzene over different morphology BiPO₄: Revealing the significant contribution of high-energy facets and oxygen vacancies, *Applied Catalysis B: Environmental*, 243 (2019) 780-789.

- [6] S.G. Babu, P. Karthik, M.C. John, S.K. Lakhera, M. Ashokkumar, J. Khim, B. Neppolian, Synergistic effect of sono-photocatalytic process for the degradation of organic pollutants using CuO-TiO₂/rGO, *Ultrasonics Sonochemistry*, 50 (2019) 218-223.
- [7] L. Parizot, T. Chave, M.-E. Galvez, H. Dutilleul, P. Da Costa, S.I. Nikitenko, Sonocatalytic oxidation of EDTA in aqueous solutions over noble metal-free Co₃O₄/TiO₂ catalyst, *Applied Catalysis B: Environmental*, 241 (2019) 570-577.
- [8] F. Chang, F. Wu, W. Yan, M. Jiao, J. Zheng, B. Deng, X. Hu, Oxygen-rich bismuth oxychloride Bi₁₂O₁₇Cl₂ materials: construction, characterization, and sonocatalytic degradation performance, *Ultrasonics Sonochemistry*, 50 (2019) 105-113.
- [9] L. Zeng, S. Li, X. Li, J. Li, S. Fan, X. Chen, Z. Yin, M. Tadé, S. Liu, Visible-light-driven sonophotocatalysis and peroxymonosulfate activation over 3D urchin-like MoS₂/C nanoparticles for accelerating levofloxacin elimination: Optimization and kinetic study, *Chemical Engineering Journal*, 378 (2019) 122039.
- [10] S. Tonda, S. Kumar, M. Bhardwaj, P. Yadav, S. Ogale, g-C₃N₄/NiAl-LDH 2D/2D hybrid heterojunction for high-performance photocatalytic reduction of CO₂ into renewable fuels, *ACS Applied Materials & Interfaces*, 10 (2018) 2667-2678.
- [11] X. Li, J. Xue, S. Ma, P. Xu, C. Huang, M. Wang, Synthesis of MgAl LDH/acidified g-C₃N₄ heterojunction photocatalyst for improved tetracycline hydrochloride degradation activity, *Nano*, 14 (2019) 1950066.
- [12] J. Ni, J. Xue, J. Shen, G. He, H. Chen, Fabrication of ZnAl mixed metal-oxides/RGO nanohybrid composites with enhanced photocatalytic activity under visible light, *Applied Surface Science*, 441 (2018) 599-606.
- [13] S. Megala, S. Prabhu, S. Harish, M. Navaneethan, S. Sohila, R. Ramesh, Enhanced photocatalytic dye degradation activity of carbonate intercalated layered Zn, ZnNi and ZnCu hydroxides, *Applied Surface Science*, 481 (2019) 385-393.

- [14] S. Yu, Z.-J. Li, X.-B. Fan, J.-X. Li, F. Zhan, X.-B. Li, Y. Tao, C.-H. Tung, L.-Z. Wu, Vectorial electron transfer for improved hydrogen evolution by mercaptopropionic-acid-regulated CdSe quantum-dots–TiO₂–Ni(OH)₂ assembly, *ChemSusChem*, 8 (2015) 642-649.
- [15] Z. Wang, G. Liu, C. Ding, Z. Chen, F. Zhang, J. Shi, C. Li, Synergetic effect of conjugated Ni(OH)₂/IrO₂ cocatalyst on titanium-doped hematite photoanode for solar water splitting, *The Journal of Physical Chemistry C*, 119 (2015) 19607-19612.
- [16] Z. Guo, W. Ye, X. Fang, J. Wan, Y. Ye, Y. Dong, D. Cao, D. Yan, Amorphous cobalt–iron hydroxides as high-efficiency oxygen-evolution catalysts based on a facile electrospinning process, *Inorganic Chemistry Frontiers*, 6 (2019) 687-693.
- [17] S. Mahzoon, M. Haghghi, S.M. Nowee, Sonoprecipitation fabrication of enhanced electron transfer Cu(OH)₂/g-C₃N₄ nanophotocatalyst with promoted H₂-production activity under visible light irradiation, *Renewable Energy*, 150 (2020) 91-100.
- [18] D. Sun, D. Chi, Z. Yang, Z. Xing, J. Yin, Z. Li, Q. Zhu, W. Zhou, Mesoporous g-C₃N₄/Zn–Ti LDH laminated van der Waals heterojunction nanosheets as remarkable visible-light-driven photocatalysts, *International Journal of Hydrogen Energy*, 44 (2019) 16348-16358.
- [19] U.M. Garusinghe, V.S. Raghuwanshi, W. Batchelor, G. Garnier, Water resistant cellulose–titanium dioxide composites for photocatalysis, *Scientific Reports*, 8 (2018) 1-13.
- [20] M.A. Mohamed, W.N.W. Salleh, J. Jaafar, A.F. Ismail, M. Abd Mutalib, S.M. Jamil, Incorporation of N-doped TiO₂ nanorods in regenerated cellulose thin films fabricated from recycled newspaper as a green portable photocatalyst, *Carbohydrate Polymers*, 133 (2015) 429-437.
- [21] L. Jiang, X. Yuan, G. Zeng, J. Liang, X. Chen, H. Yu, H. Wang, Z. Wu, J. Zhang, T. Xiong, In-situ synthesis of direct solid-state dual Z-scheme WO₃/g-C₃N₄/Bi₂O₃ photocatalyst for the degradation of refractory pollutant, *Applied Catalysis B: Environmental*, 227 (2018) 376-385.

- [22] S. Bi, C. Wang, Q. Cao, C. Zhang, Studies on the mechanism of hydrolysis and polymerization of aluminum salts in aqueous solution: correlations between the “Core-links” model and “Cage-like” Keggin- Al_{13} model, *Coordination Chemistry Reviews*, 248 (2004) 441-455.
- [23] M. Karpuraranjith, Y. Chen, X. Wang, B. Yu, S. Rajaboopathi, D. Yang, Hexagonal SnSe nanoplate supported SnO₂-CNTs nanoarchitecture for enhanced photocatalytic degradation under visible light driven, *Applied Surface Science*, 507 (2020) 145026.
- [24] A. Khataee, B. Kayan, P. Gholami, D. Kalderis, S. Akay, L. Dinpazhoh, Sonocatalytic degradation of Reactive Yellow 39 using synthesized ZrO₂ nanoparticles on biochar, *Ultrasonics Sonochemistry*, 39 (2017) 540-549.
- [25] Water Environment Federation (WEF) , American Public Health Association (APHA), American Water Works Association (AWWA), Standard methods for the examination of water and wastewater (21st ed.), 2005, Washington, D. C., USA.
- [26] S. Ozden, S. Bawari, S. Vinod, U. Martinez, S. Susarla, C. Narvaez, J. Joyner, C.S. Tiwary, T.N. Narayanan, P.M. Ajayan, Interface and defect engineering of hybrid nanostructures toward an efficient HER catalyst, *Nanoscale*, 11 (2019) 12489-12496.
- [27] H. Kuroki, S. Miyanishi, A. Sakakibara, Y. Oshiba, T. Yamaguchi, Highly stable membrane–electrode assembly using ether-linkage-free spirobifluorene-based aromatic polyelectrolytes for direct formate solid alkaline fuel cells, *Journal of Power Sources*, 438 (2019) 226997.
- [28] W. Chen, G. Qing, T. Sun, A novel aggregation-induced emission enhancement triggered by the assembly of a chiral gelator: from non-emissive nanofibers to emissive micro-loops, *Chemical Communications*, 53 (2017) 447-450.

- [29] S. Mondal, P. Chakraborty, P. Bairi, D.P. Chatterjee, A.K. Nandi, Light induced E–Z isomerization in a multi-responsive organogel: elucidation from ¹H NMR spectroscopy, *Chemical Communications*, 51 (2015) 10680-10683.
- [30] M. Hashmi, Q. Sun, J. Tao, T. Wells, A.A. Shah, N. Labbé, A.J. Ragauskas, Comparison of autohydrolysis and ionic liquid 1-butyl-3-methylimidazolium acetate pretreatment to enhance enzymatic hydrolysis of sugarcane bagasse, *Bioresource Technology*, 224 (2017) 714-720.
- [31] M. Wang, J. Ma, C. Chen, X. Zheng, Z. Du, J. Xu, Preparation of self-assembled cobalt hydroxide nanoflowers and the catalytic decomposition of cyclohexyl hydroperoxide, *Journal of Materials Chemistry*, 21 (2011) 12609-12612.
- [32] P. Gholami, A. Khataee, R.D.C. Soltani, L. Dinpazhoh, A. Bhatnagar, Photocatalytic degradation of gemifloxacin antibiotic using Zn-Co-LDH@biochar nanocomposite, *Journal of Hazardous Materials*, 382 (2020) 121070.
- [33] K.M. Parida, L. Mohapatra, Carbonate intercalated Zn/Fe layered double hydroxide: A novel photocatalyst for the enhanced photo degradation of azo dyes, *Chemical Engineering Journal*, 179 (2012) 131-139.
- [34] J. Tauc, Optical properties and electronic structure of amorphous Ge and Si, *Materials Research Bulletin*, 3 (1968) 37-46.
- [35] J.R. Kim, E. Kan, Heterogeneous photocatalytic degradation of sulfamethoxazole in water using a biochar-supported TiO₂ photocatalyst, *Journal of Environmental Management*, 180 (2016) 94-101.
- [36] Z. Li, Y. Wu, G. Lu, Highly efficient hydrogen evolution over Co(OH)₂ nanoparticles modified g-C₃N₄ co-sensitized by Eosin Y and Rose Bengal under visible light irradiation, *Applied Catalysis B: Environmental*, 188 (2016) 56-64.

- [37] M. Seredych, S. Łoś, D.A. Giannakoudakis, E. Rodríguez-Castellón, T.J. Bandoz, Photoactivity of g-C₃N₄/S-doped porous carbon composite: Synergistic effect of composite formation, *ChemSusChem*, 9 (2016) 795-799.
- [38] N. Geng, W. Chen, H. Xu, M. Ding, Z. Liu, Z. Shen, A sono-photocatalyst for humic acid removal from water: Operational parameters, kinetics and mechanism, *Ultrasonics Sonochemistry*, 57 (2019) 242-252.
- [39] J. Qiao, M. Lv, Z. Qu, M. Zhang, X. Cui, D. Wang, C. Piao, Z. Liu, J. Wang, Y. Song, Preparation of a novel Z-scheme KTaO₃/FeVO₄/Bi₂O₃ nanocomposite for efficient sonocatalytic degradation of ceftriaxone sodium, *Science of The Total Environment*, 689 (2019) 178-192.
- [40] M. Vaez, A. Zarringhalam Moghaddam, S. Alijani, Optimization and modeling of photocatalytic degradation of Azo dye using a response surface methodology (RSM) based on the central composite design with immobilized titania nanoparticles, *Industrial & Engineering Chemistry Research*, 51 (2012) 4199-4207.
- [41] E. Selli, Synergistic effects of sonolysis combined with photocatalysis in the degradation of an azo dye, *Physical Chemistry Chemical Physics*, 4 (2002) 6123-6128.
- [42] M. Tobajas, C. Belver, J.J. Rodriguez, Degradation of emerging pollutants in water under solar irradiation using novel TiO₂-ZnO/clay nanoarchitectures, *Chemical Engineering Journal*, 309 (2017) 596-606.
- [43] N. Sabzroo, T.R. Bastami, M. Karimi, T. Heidari, S. Agarwal, V.K. Gupta, Synthesis and characterization of magnetic poly(acrylonitrile-co-acrylic acid) nanofibers for dispersive solid phase extraction and pre-concentration of malachite green from water samples, *Journal of Industrial and Engineering Chemistry*, 60 (2018) 237-249.

- [44] M. Mohajerani, M. Mehrvar, F. Ein-Mozaffari, Using an external-loop airlift sonophotoreactor to enhance the biodegradability of aqueous sulfadiazine solution, *Separation and Purification Technology*, 90 (2012) 173-181.
- [45] W. Ding, M. Sun, Z. Zhang, X. Lin, B. Gao, Ultrasound-promoted synthesis of γ -graphyne for supercapacitor and photoelectrochemical applications, *Ultrasonics Sonochemistry*, 61 (2020) 104850.
- [46] R. Darvishi Cheshmeh Soltani, M. Safari, M. Mashayekhi, Sonocatalyzed decolorization of synthetic textile wastewater using sonochemically synthesized MgO nanostructures, *Ultrasonics Sonochemistry*, 30 (2016) 123-131.
- [47] L.W. Matzek, K.E. Carter, Activated persulfate for organic chemical degradation: A review, *Chemosphere*, 151 (2016) 178-188.
- [48] W.-D. Oh, Z. Dong, T.-T. Lim, Hierarchically-structured Co-CuBi₂O₄ and Cu-CuBi₂O₄ for sulfanilamide removal via peroxymonosulfate activation, *Catalysis Today*, 280 (2017) 2-7.
- [49] Q. Wang, B. Wang, Y. Ma, S. Xing, Enhanced superoxide radical production for ofloxacin removal via persulfate activation with Cu-Fe oxide, *Chemical Engineering Journal*, 354 (2018) 473-480.
- [50] C. Lops, A. Ancona, K. Di Cesare, B. Dumontel, N. Garino, G. Canavese, S. Hernández, V. Cauda, Sonophotocatalytic degradation mechanisms of Rhodamine B dye via radicals generation by micro- and nano-particles of ZnO, *Applied Catalysis B: Environmental*, 243 (2019) 629-640.
- [51] W.-K. Jo, S. Tonda, Novel CoAl-LDH/g-C₃N₄/RGO ternary heterojunction with notable 2D/2D/2D configuration for highly efficient visible-light-induced photocatalytic elimination of dye and antibiotic pollutants, *Journal of Hazardous Materials*, 368 (2019) 778-787.

- [52] J. Sun, X. Yan, K. Lv, S. Sun, K. Deng, D. Du, Photocatalytic degradation pathway for azo dye in TiO₂/UV/O₃ system: Hydroxyl radical versus hole, *Journal of Molecular Catalysis A: Chemical*, 367 (2013) 31-37.
- [53] A. Khataee, P. Gholami, B. Kayan, D. Kalderis, L. Dinpazhoh, S. Akay, Synthesis of ZrO₂ nanoparticles on pumice and tuff for sonocatalytic degradation of rifampin, *Ultrasonics Sonochemistry*, 48 (2018) 349-361.
- [54] R. Lu, X. Xu, J. Chang, Y. Zhu, S. Xu, F. Zhang, Improvement of photocatalytic activity of TiO₂ nanoparticles on selectively reconstructed layered double hydroxide, *Applied Catalysis B: Environmental*, 111-112 (2012) 389-396.
- [55] Y. Ao, D. Wang, P. Wang, C. Wang, J. Hou, J. Qian, Enhanced photocatalytic properties of the 3D flower-like Mg-Al layered double hydroxides decorated with Ag₂CO₃ under visible light illumination, *Materials Research Bulletin*, 80 (2016) 23-29.
- [56] H. Zhang, Z. Wang, R. Li, J. Guo, Y. Li, J. Zhu, X. Xie, TiO₂ supported on reed straw biochar as an adsorptive and photocatalytic composite for the efficient degradation of sulfamethoxazole in aqueous matrices, *Chemosphere*, 185 (2017) 351-360.
- [57] H. Lin, J. Niu, J. Xu, Y. Li, Y. Pan, Electrochemical mineralization of sulfamethoxazole by Ti/SnO₂-Sb/Ce-PbO₂ anode: Kinetics, reaction pathways, and energy cost evolution, *Electrochim. Acta*, 97 (2013) 167-174.

Figures captions

Fig. 1. (a) XRD patterns (the black, blue, brown and green colors in the XRD patterns indicate the lattice planes of g-C₃N₄, orthorhombic Cu(OH)₂, hexagonal brucite Mg(OH)₂ and

orthorhombic $\text{Zn}(\text{OH})_2$, respectively.), (b) FT-IR spectra, (c) N_2 adsorption–desorption isotherms, (d) $(\alpha h\nu)^2-h\nu$ plots, and (e) PL spectra of the samples.

Fig. 2. SEM images of (a-c) g- C_3N_4 , (d-f) MMH, (g-i) MMH/g- C_3N_4 , (j and k) pure MFC and (l-o) MMH/g- C_3N_4 @MFC₃ samples.

Fig. 3. EDX dot mapping micrographs of MFC (a1-a3), MMH/g- C_3N_4 @MFC₁ (b1-b6), MMH/g- C_3N_4 @MFC₂ (c1-c6), and MMH/g- C_3N_4 @MFC₃ (d1-d6).

Fig. 4. (a) Comparative evaluation of performance of different processes in the SDZ degradation; (b) the related kinetic analysis based on the pseudo-first-order model (A: photolysis, B: sonolysis, C: sonophotolysis, D, E and F: sonophotocatalysis using MMH, g- C_3N_4 and MMH/g- C_3N_4 , respectively); (c) Comparative evaluation of sonophotocatalytic performance of MFC-based films and (d) related kinetic analysis based on the pseudo-first-order model (A: bare MFC, B: MMH/g- C_3N_4 @MFC₁, C: MMH/g- C_3N_4 @MFC₂ and D: MMH/g- C_3N_4 @MFC₃); Experimental conditions: $[\text{SDZ}]_0 = 0.15 \text{ mM}$, catalyst dosage = 0.5 g L^{-1} , the dimensions of the catalysts strips = $2.5 \text{ cm} \times 2.5 \text{ cm}$, pH = 6.5 (natural pH), and ultrasonic power = 300 W.

Fig. 5. Effect of operational variables on the degradation efficiency of SDZ; (a) effect of SDZ concentration (the dimensions of the MMH/g- C_3N_4 @MFC₃ strip = $2.5 \text{ cm} \times 2.5 \text{ cm}$, pH = 6.5, and ultrasonic power = 300 W); (b) effect of pH (the dimensions of the MMH/g- C_3N_4 @MFC₃ strip = $2.5 \text{ cm} \times 2.5 \text{ cm}$, $[\text{SDZ}]_0 = 0.15 \text{ mM}$, and ultrasonic power = 300 W), and (d) effect of ultrasonic power (the dimensions of the MMH/g- C_3N_4 @MFC₃ strip = $2.5 \text{ cm} \times 2.5 \text{ cm}$, $[\text{SDZ}]_0 = 0.15 \text{ mM}$, and pH = 6.5).

Fig. 6. DE% of SDZ through sonophotocatalysis in the presence of (a) various oxidants (the dimensions of the MMH/g- C_3N_4 @MFC₃ strip = $2.5 \text{ cm} \times 2.5 \text{ cm}$, $[\text{SDZ}]_0 = 0.30 \text{ mM}$, pH = 6.5, ultrasonic power = 300 W and $[\text{oxidant}] = 5 \text{ mM}$), (b) organic scavengers, and (c) inorganic

scavengers, (the dimensions of the MMH/g-C₃N₄@MFC₃ strip =2.5 cm × 2.5 cm, [SDZ]₀ = 0.15 mM, pH = 6.5, ultrasonic power = 300 W and [scavenger] = 5 mM).

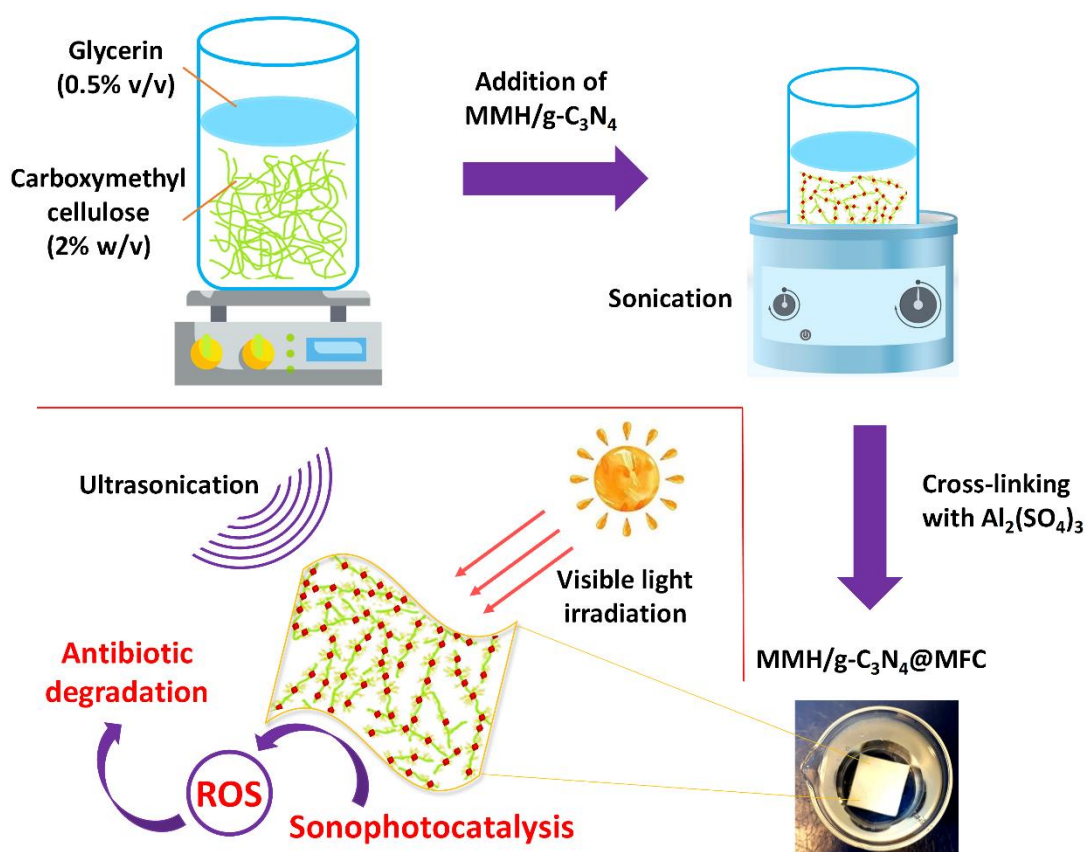
Fig. 7. Proposed routes for sonophotocatalytic degradation of SDZ using MMH/g-C₃N₄@MFC₃ catalyst.

Fig. 8. Degradation efficiency for ten consecutive sonophotocatalytic degradation experiments; Experimental conditions: the dimensions of the MMH/g-C₃N₄@MFC₃ strip =2.5 cm × 2.5 cm, [SDZ]₀ = 0.15 mM, pH = 6.5 and ultrasonic power = 300 W.

Highlights

- Synthesis of Zn-Cu-Mg mixed metal hydroxide/g-C₃N₄ photocatalyst
- Integration of the photocatalyst with microfibrillated carboxymethyl cellulose
- Sonophotocatalytic degradation of sulfadiazine using the fabricated composite
- Reusability of the prepared composite after ten sonophotocatalytic cycles
- A possible pathway for sonophotocatalytic degradation of sulfadiazine

Graphical Abstract



Fabrication of water resistant Zn-Cu-Mg mixed metal hydroxide/g-C₃N₄ modified microfibrillated carboxymethyl cellulose for sonophotocatalytic degradation of sulfadiazine.

Figures

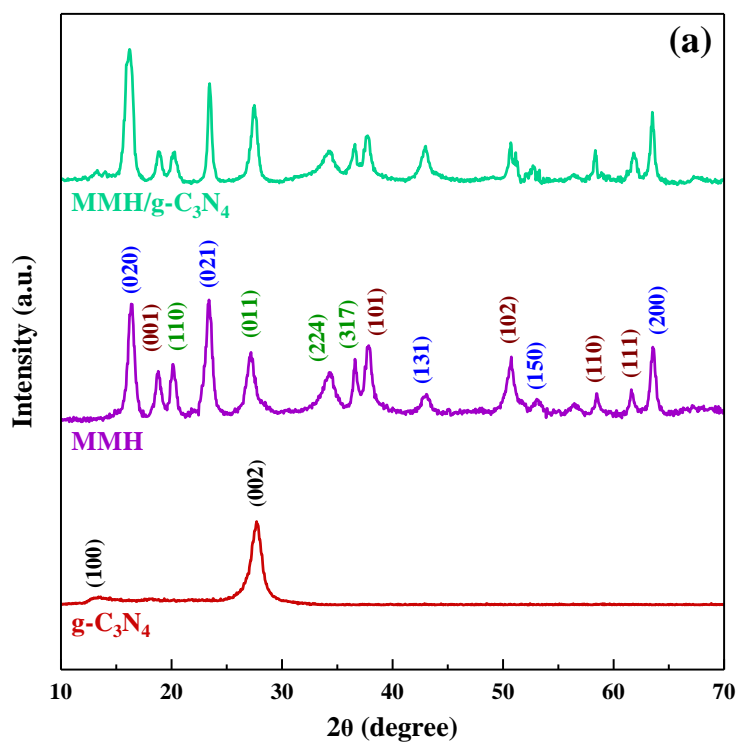


Fig. 1 (a)

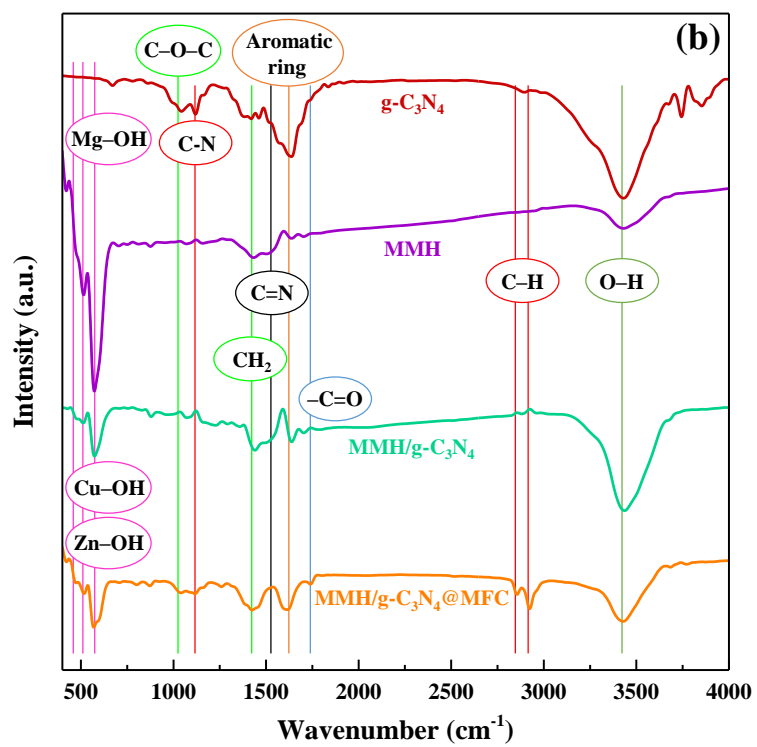


Fig. 1 (b)

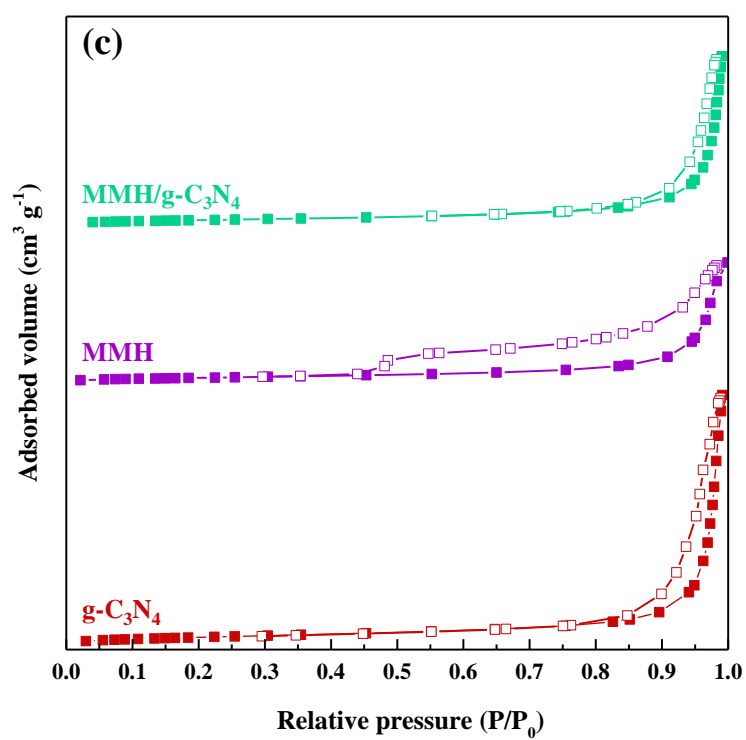


Fig. 1 (c)

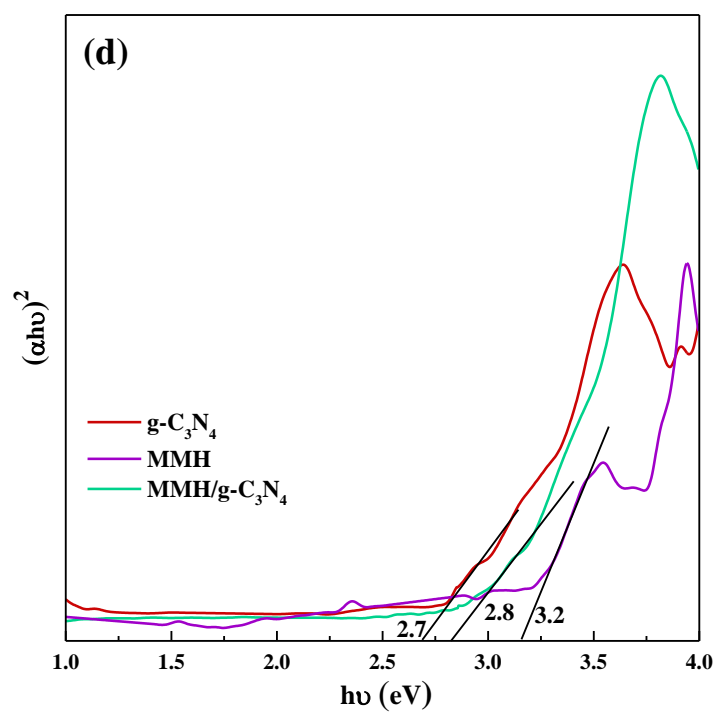


Fig. 1 (d)

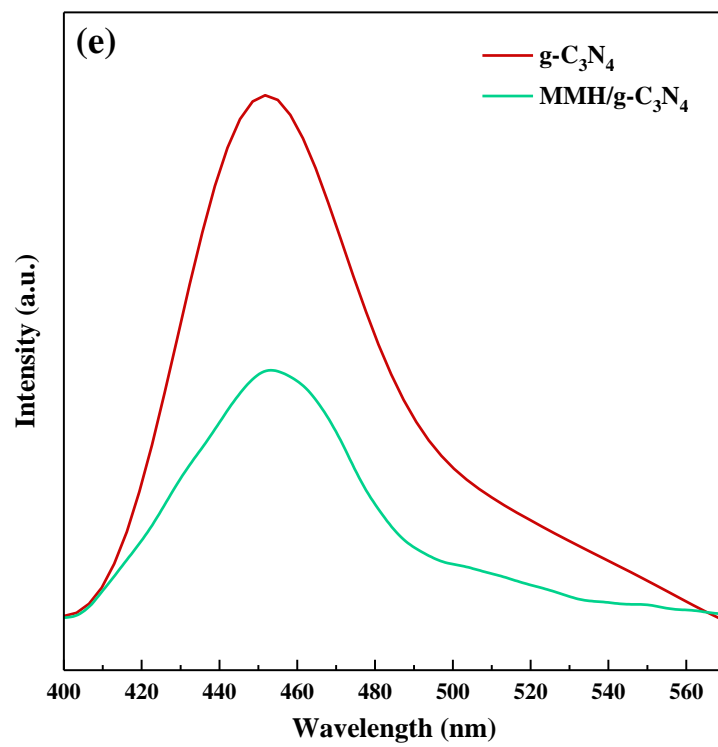


Fig. 1 (e)

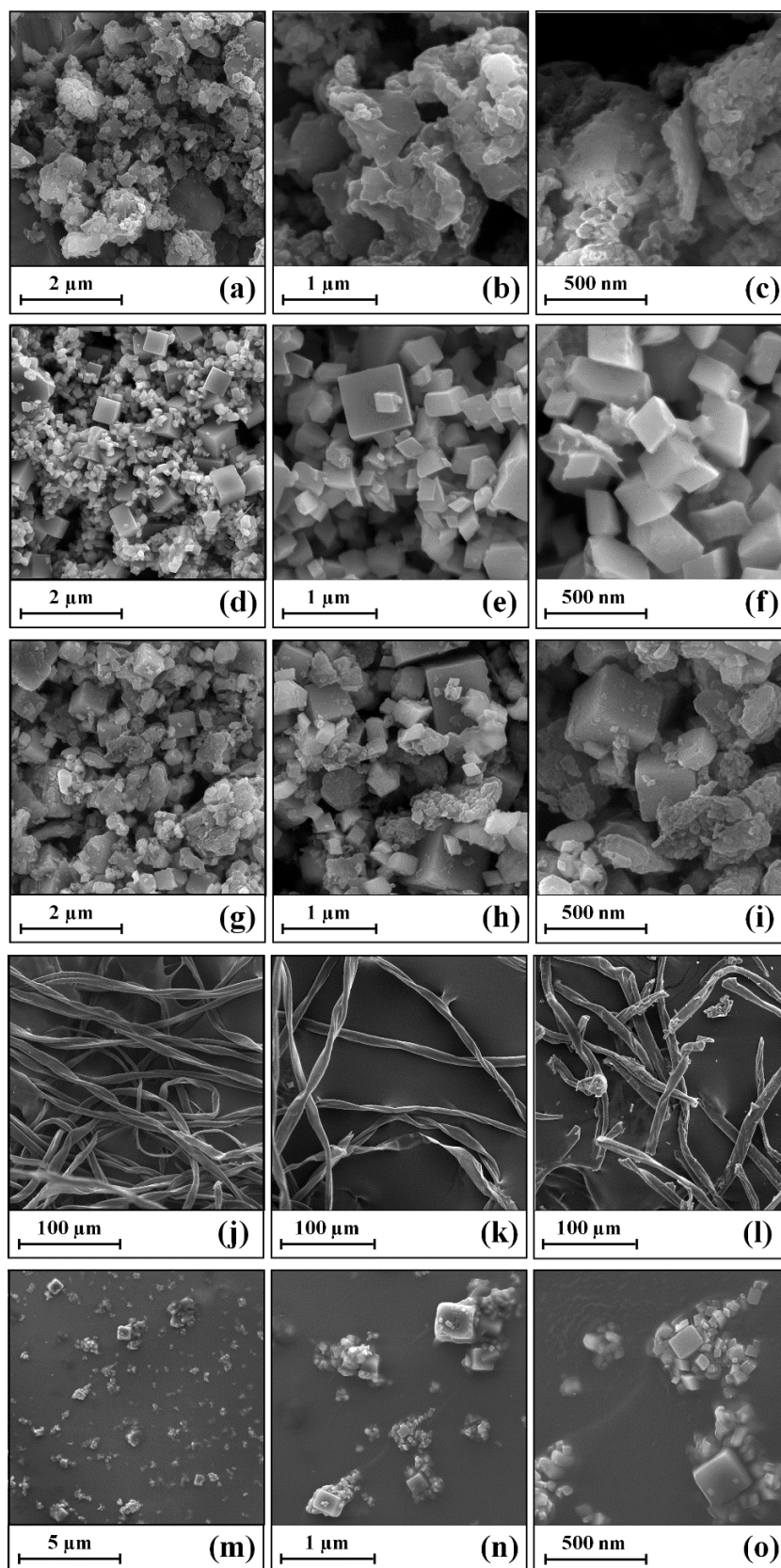


Fig. 2

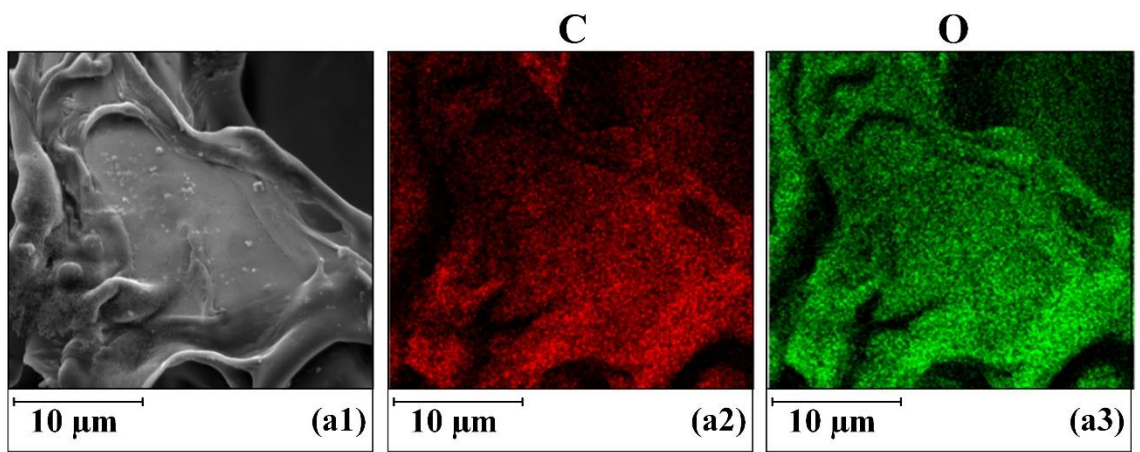


Fig. 3 (a1-a3)

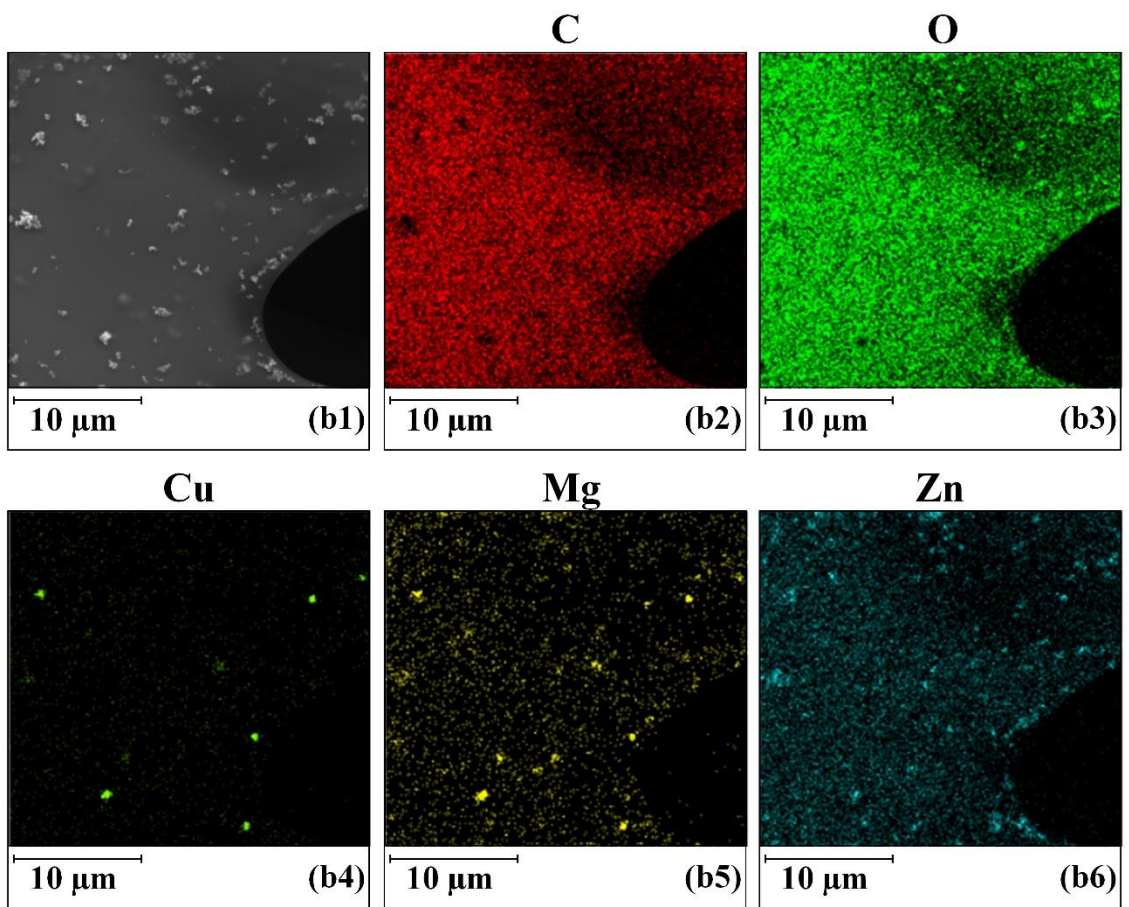


Fig. 3 (b1-b3)

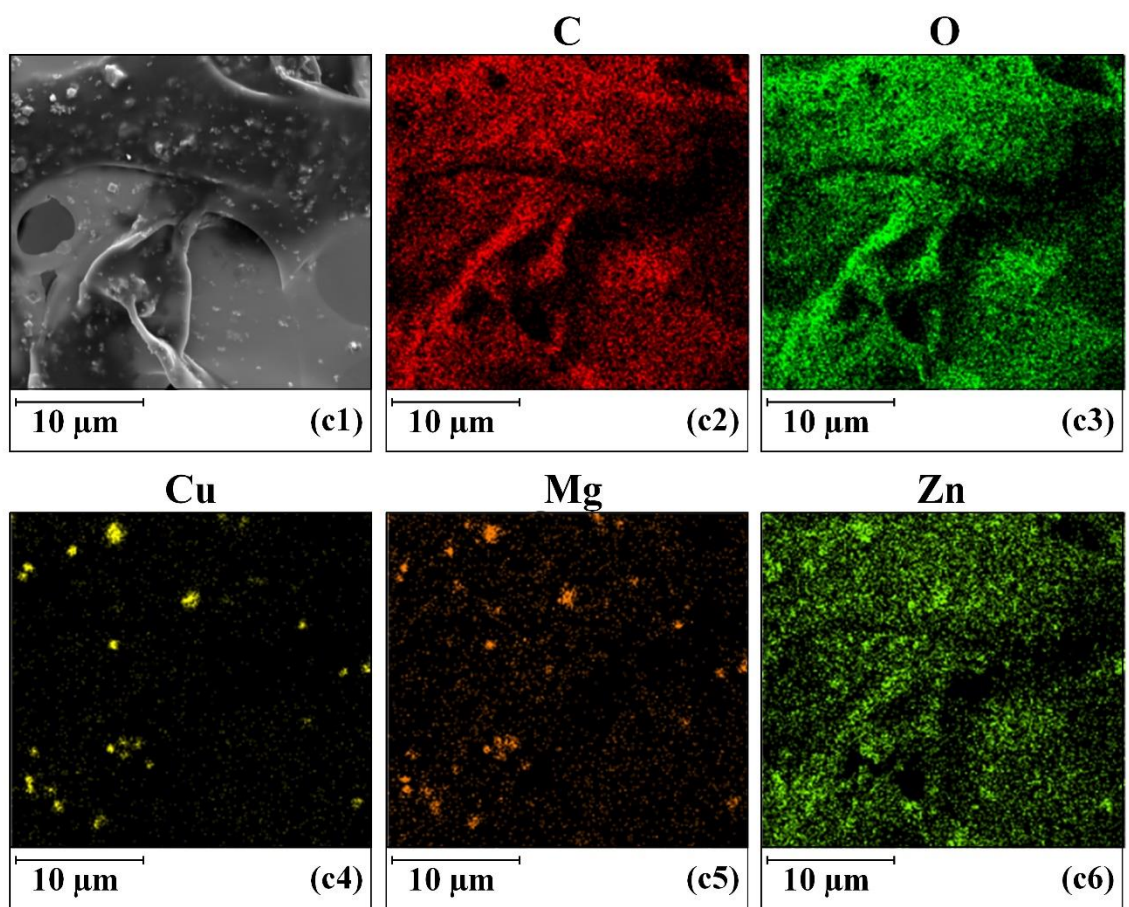


Fig. 3 (c1-c3)

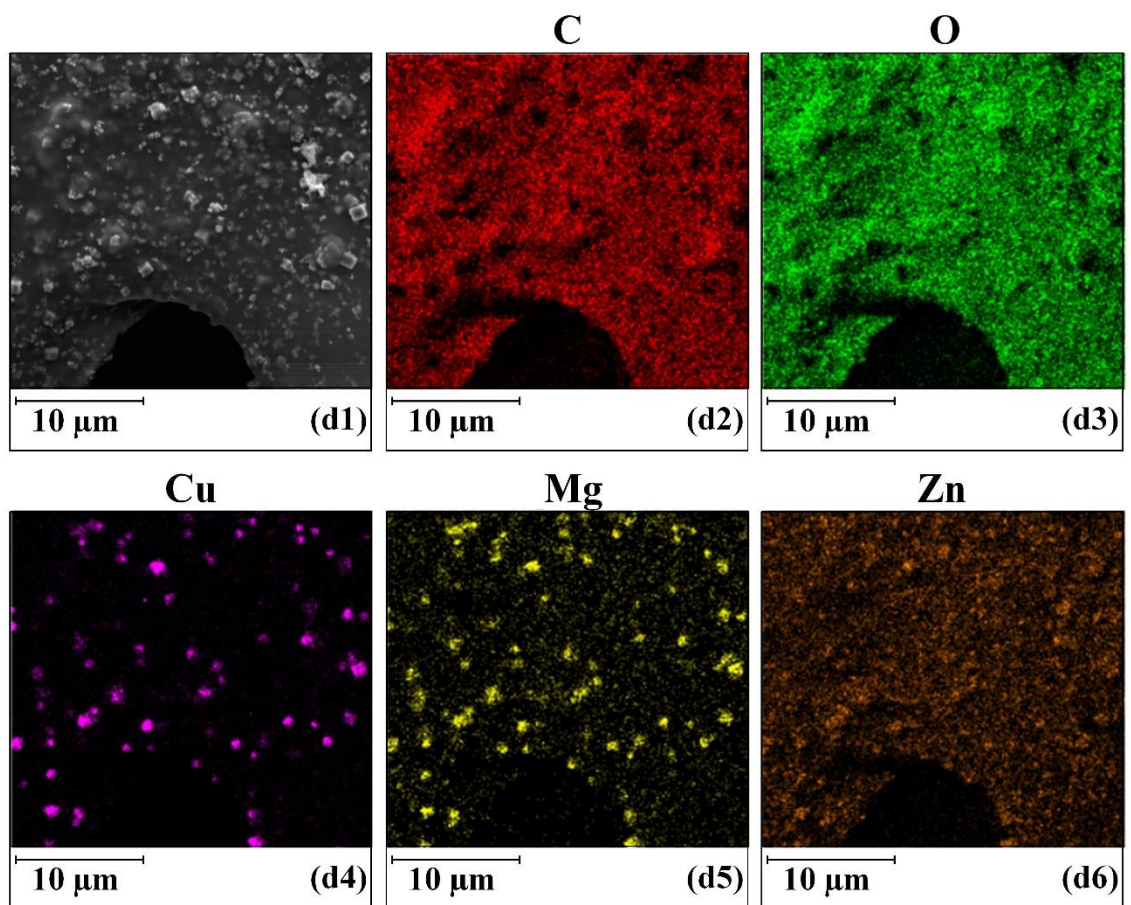


Fig. 3 (cd1-cd)

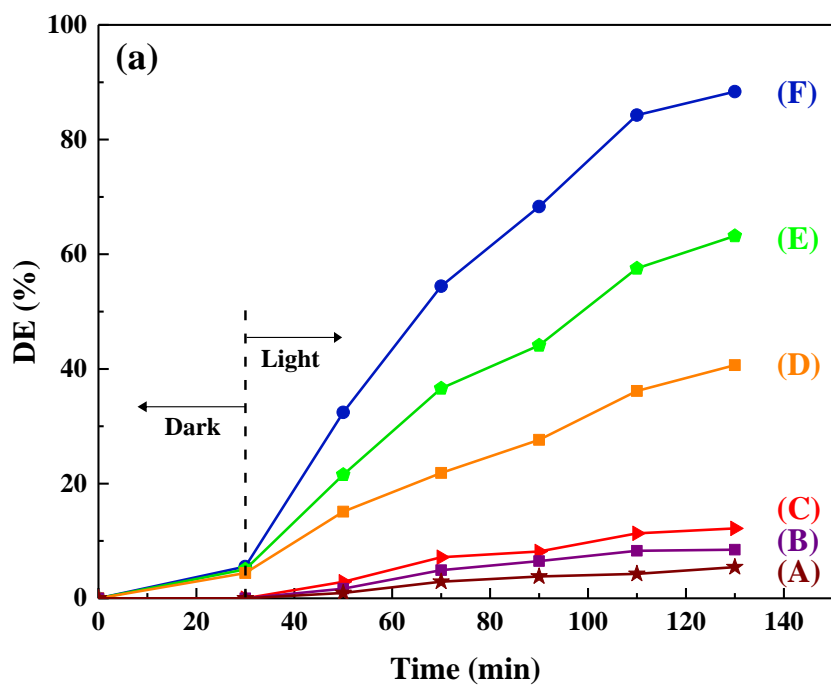


Fig. 4 (a)

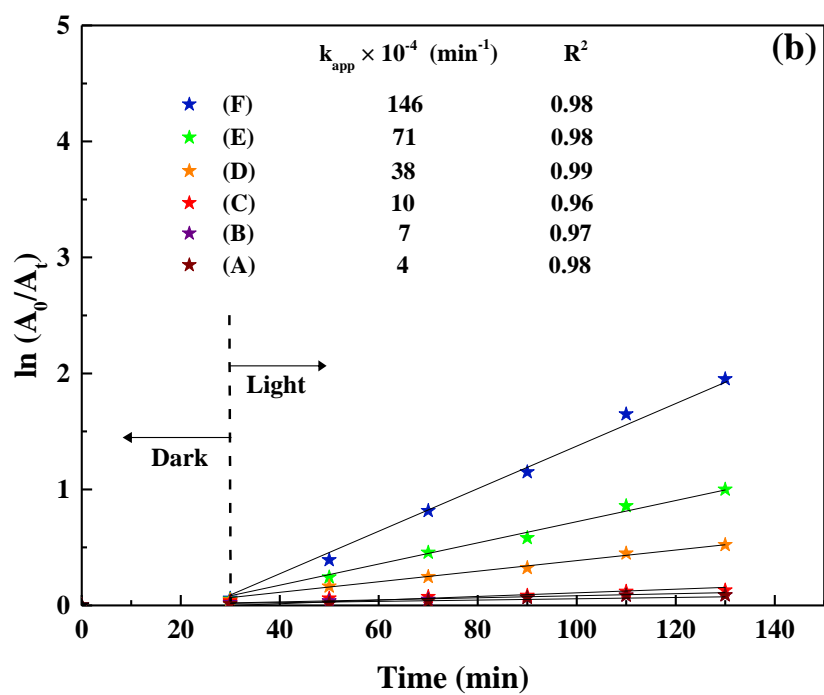


Fig. 4 (b)

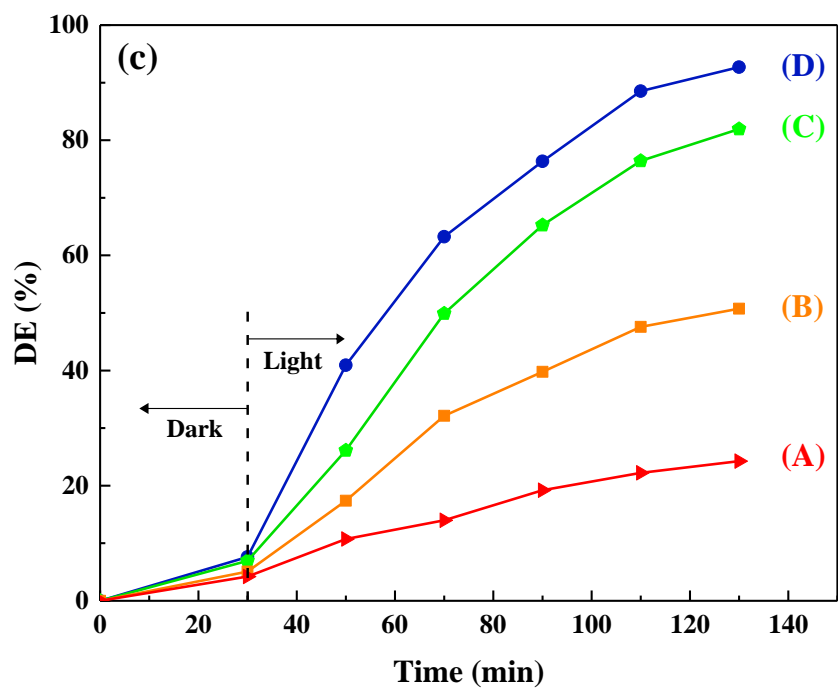


Fig. 4 (c)

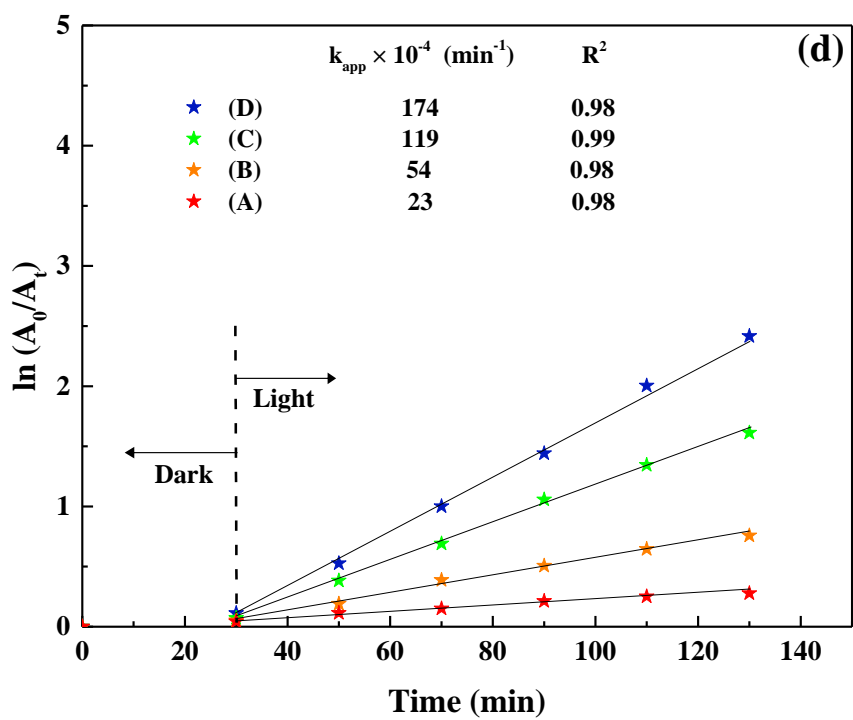


Fig. 4 (d)

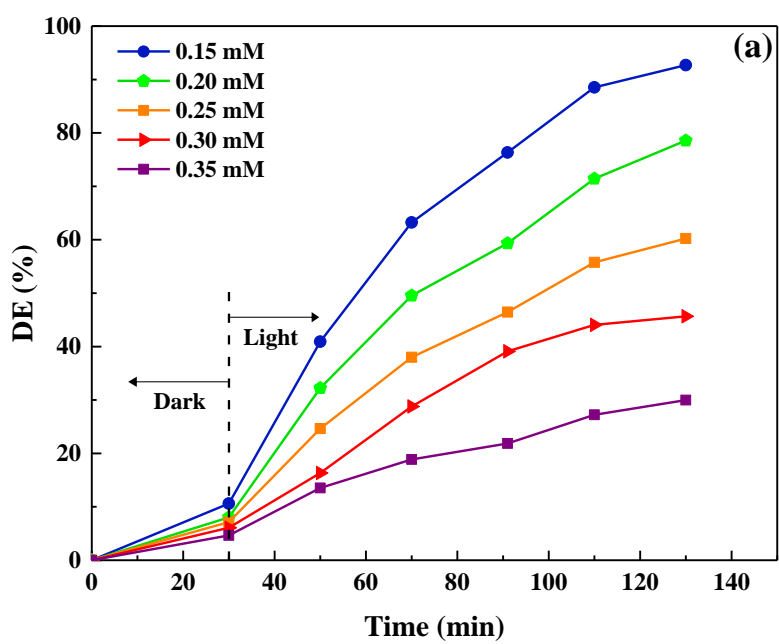


Fig. 5 (a)

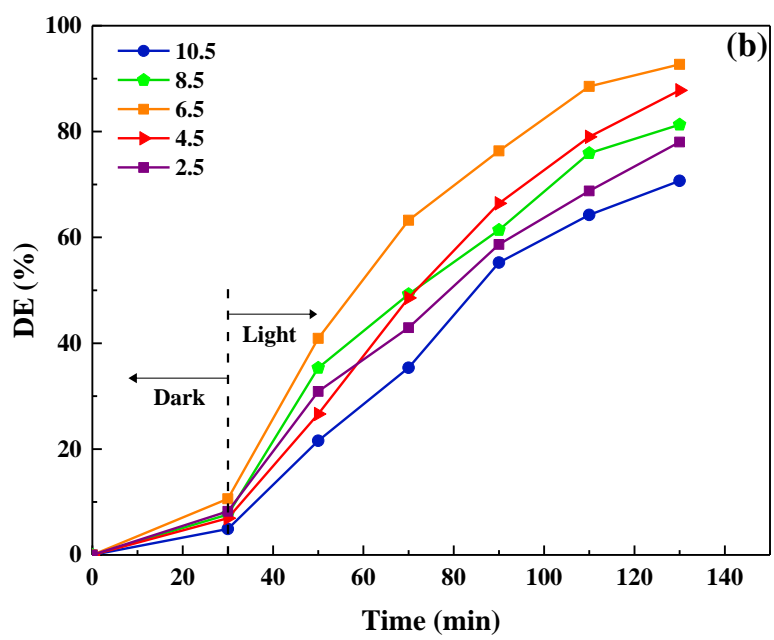


Fig. 5 (b)

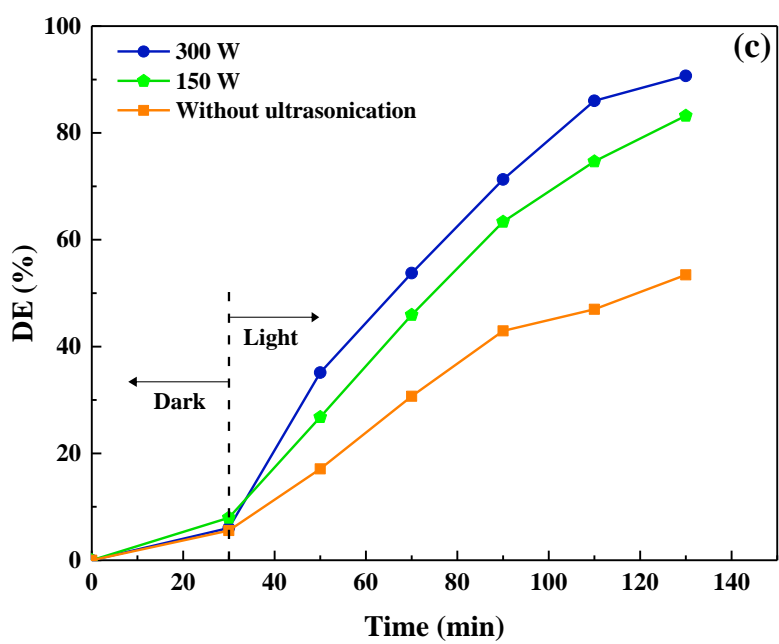


Fig. 5 (c)

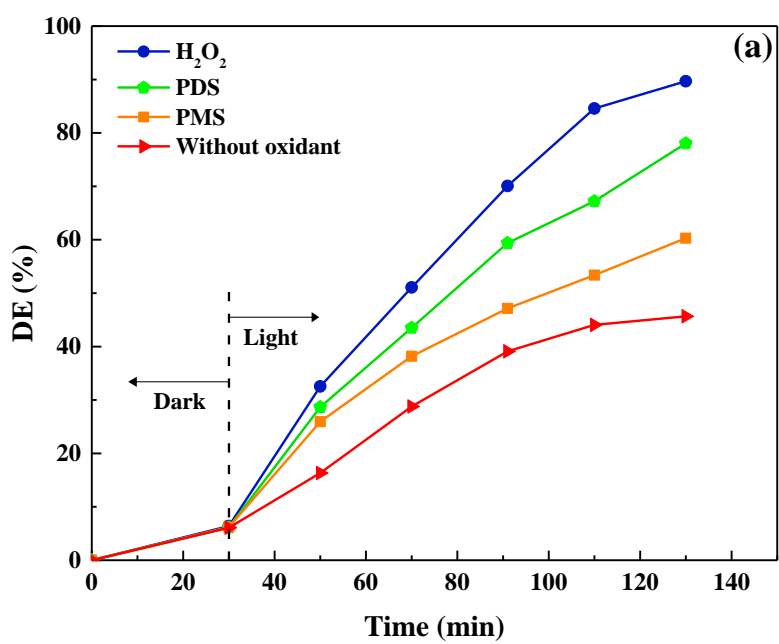


Fig. 6 (a)

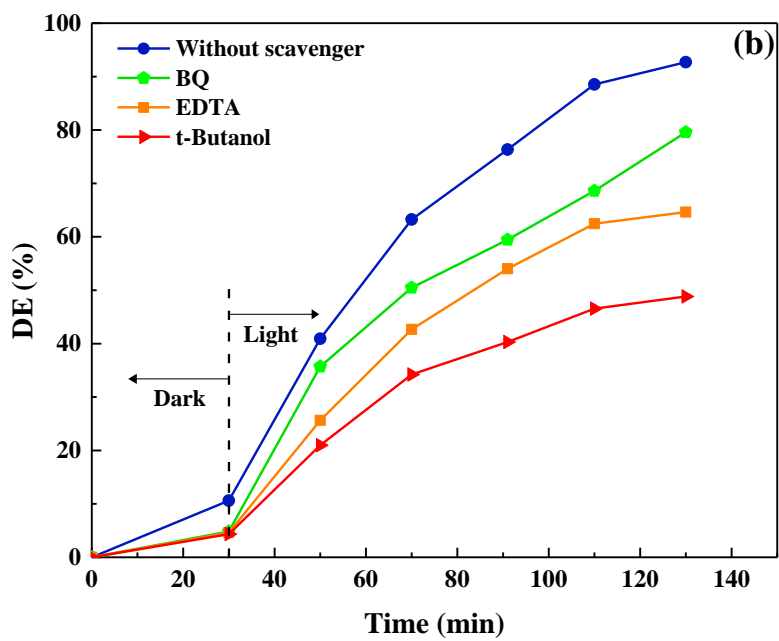


Fig. 6 (b)

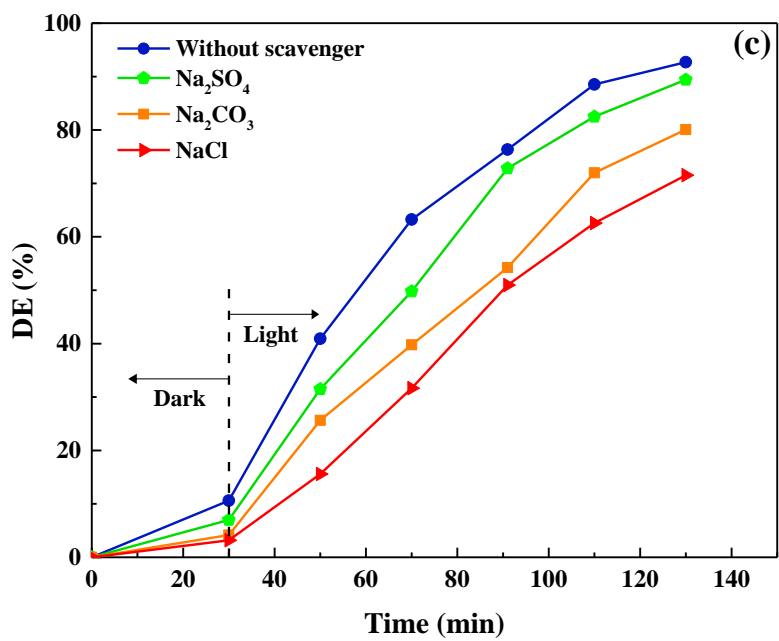


Fig. 6 (c)

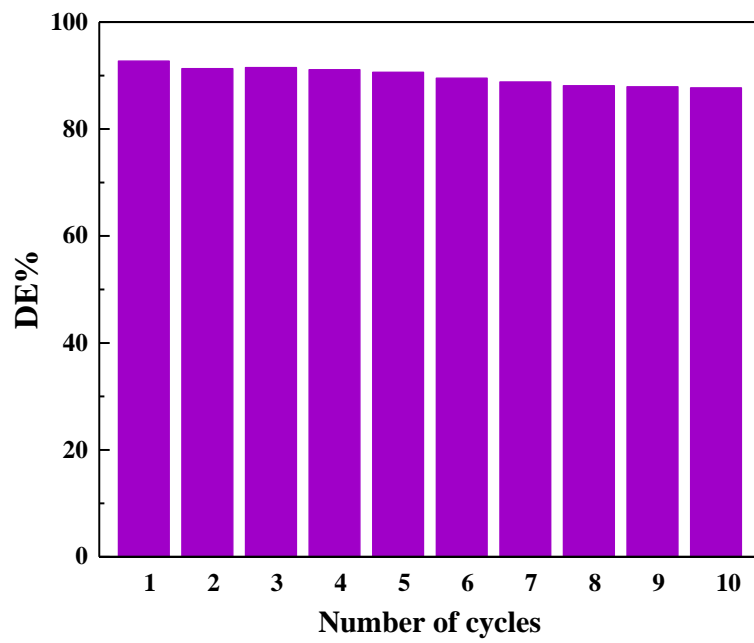


Fig. 7

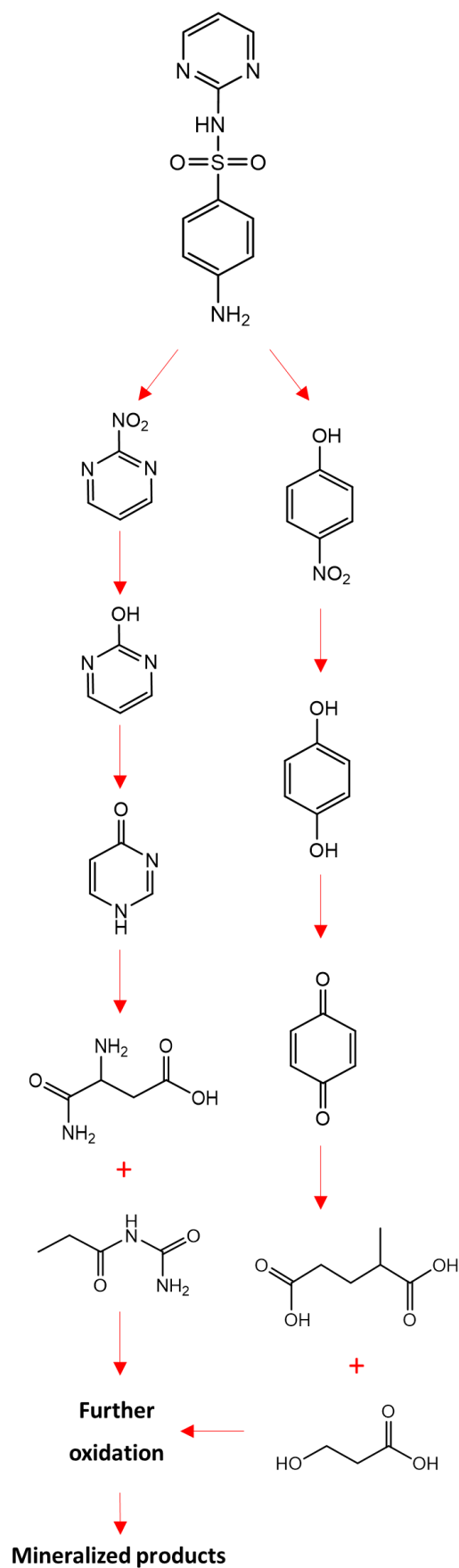


Fig. 8

Supplementary data

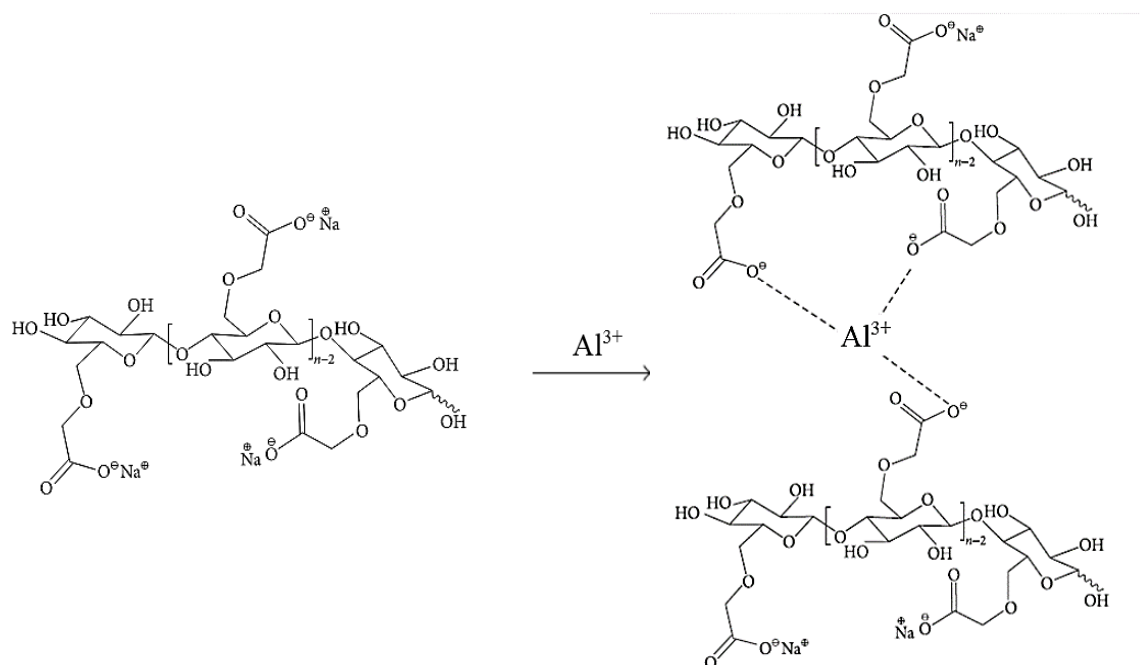
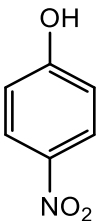
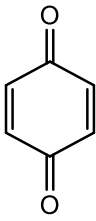
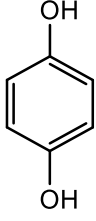
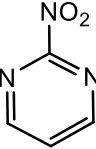
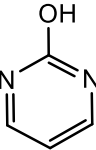
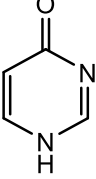
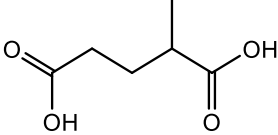


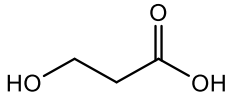
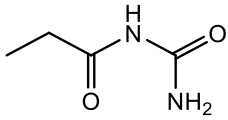
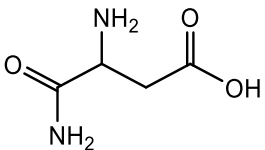
Fig. S1. The general mechanism of ionic crosslinking between carboxylate groups of carboxymethyl cellulose and Al^{3+} crosslinker.

Table S1. Chemical composition of the samples as measured by EDX analysis.

Sample	C (w%)	O (w%)	Cu (w%)	Mg (w%)	Zn (w%)
Pure MFC	48	52	-	-	-
MMH/g-C ₃ N ₄ @MFC ₁	42	51	1	2	4
MMH/g-C ₃ N ₄ @MFC ₂	39	47	2	4	8
MMH/g-C ₃ N ₄ @MFC ₃	35	45	3	7	10

Table S2. Identified intermediate compounds produced during degradation of SDZ.

No.	Compound name	Structure	Retention time (min)	Main fragments
1	4-Nitrophenol		14.721	39 (23%), 65 (100%), 109 (59%), 139 (54%)
2	Cyclohexa-2,5-diene-1,4-dione		11.852	26 (18%), 54 (71), 82 (29%), 108 (100%)
3	Benzene-1,4-diol		12.064	39 (21%), 55 (38), 81 (41%), 110 (100%)
4	2-Nitropyrimidin		22.624	43(25%), 84(39%), 94 (62%), 125 (100%)
5	1H-pyrimidin-2-one		19.816	28 (26%), 41 (35%), 68 (63%), 96 (100%)
6	4(1H)-Pyrimidinone		19.354	28(34%), 52(19%), 68 (43%), 96 (100%)
7	2-Methylpentanedioic acid		17.715	41 (31%), 56 (45%), 100 (100%), 128 (36%)

8	3-Hydroxypropanoic acid		10.369	31 (27%), 42 (51), 60 (100%), 72 (43%)
9	N-carbamoylpropanamide		18.627	29 (37%), 44 (100%), 57 (31%), 73 (25%)
10	(3S)-3,4-diamino-4-oxobutanoic acid		19.027	43 (51%), 70 (43%), 88 (100%)
